ADVANCING EARTH AND SPACE SCIENCES

JGR Atmospheres

RESEARCH ARTICLE
10.1029/2023JD040473

Assessing the Fidelity of Landfalling Tropical Cyclone Convective-Scale Environments in the Warn-On-Forecast System Using Radiosondes

Benjamin A. Schenkel[1,2,3], **Thomas Jones**[1,2,3], **and Sean Waugh**[2]

[1]Cooperative Institute for Severe and High-Impact Weather Research and Operations, Norman, OK, USA, [2]NOAA/OAR National Severe Storms Laboratory, Norman, OK, USA, [3]School of Meteorology, University of Oklahoma, Norman, OK, USA

Key Points:

- Warn-on-Forecast tropical cyclone forecasts show reasonable agreement between observed and forecast convective-scale kinematic environments
- Forecast convective-scale thermodynamic environments also show reasonable fidelity compared to observations
- A case study shows stronger discrepancies than the full sample including weaker than observed winds, temperature inversions, and dry layers

Correspondence to:

B. A. Schenkel,
benschenkel@gmail.com

Citation:

Schenkel, B. A., Jones, T., & Waugh, S. (2024). Assessing the fidelity of landfalling tropical cyclone convective-scale environments in the Warn-on-Forecast System using radiosondes. *Journal of Geophysical Research: Atmospheres*, *129*, e2023JD040473. https://doi.org/10.1029/2023JD040473

Received 29 NOV 2023
Accepted 16 MAY 2024

Author Contributions:

Conceptualization: Benjamin A. Schenkel, Thomas Jones
Data curation: Thomas Jones, Sean Waugh
Formal analysis: Benjamin A. Schenkel, Thomas Jones
Funding acquisition: Thomas Jones
Investigation: Benjamin A. Schenkel
Methodology: Benjamin A. Schenkel, Thomas Jones
Project administration: Thomas Jones
Resources: Thomas Jones, Sean Waugh
Software: Benjamin A. Schenkel
Supervision: Benjamin A. Schenkel, Thomas Jones
Validation: Benjamin A. Schenkel
Visualization: Benjamin A. Schenkel
Writing – original draft: Benjamin A. Schenkel
Writing – review & editing: Benjamin A. Schenkel, Thomas Jones

Abstract

Forecasts of tropical cyclone (TC) tornadoes are less skillful than their non-TC counterparts at all lead times. The development of a convection-allowing regional ensemble, known as the Warn-on-Forecast System (WoFS), may help improve short-fused TC tornado forecasts. As a first step, this study investigates the fidelity of convective-scale kinematic and thermodynamic environments to a preliminary set of soundings from WoFS forecasts for comparison with radiosondes for selected 2020 landfalling TCs. Our study shows reasonable agreement between TC convective-scale kinematic environments in WoFS versus observed soundings at all forecast lead times. Nonetheless, WoFS is biased toward weaker than observed TC-relative radial winds, and stronger than observed near-surface tangential winds with weaker winds aloft, during the forecast. Analysis of storm-relative helicity (SRH) shows that WoFS underestimates extreme observed values. Convective-scale thermodynamic environments are well simulated for both temperature and dewpoint at all lead times. However, WoFS is biased moister with steeper lapse rates compared to observations during the forecast. Both CAPE and, to a lesser extent, 0–3-km CAPE distributions are narrower in WoFS than in radiosondes, with an underestimation of higher CAPE values. Together, these results suggest that WoFS may have utility for forecasting convective-scale environments in landfalling TCs with lead times of several hours.

Plain Language Summary

Landfalling tropical cyclones (known as tropical depressions, tropical storms, or hurricanes) often spawn tornadoes, which are more challenging to forecast than Great Plains tornadoes. The development of a weather forecast ensemble model, known as the Warn-on-Forecast system, may help improve tornado forecasts. This study compares vertical profiles of winds, temperature, moisture, and associated severe weather metrics from the Warn-on-Forecast with observed radiosonde data (i.e., balloon-borne instruments) in landfalling tropical cyclones. Our analysis shows agreement between the observed and forecasted vertical structure of TC winds at all lead times including strong changes in near-surface wind speed and direction. Nonetheless, forecasted tropical cyclone winds tend to be biased weaker than observed, which is associated with an underestimation of environmental favorability for tornadoes. Similarly, forecasted temperature and moisture are also reasonably represented compared to observations. However, Warn-on-Forecast tends to overestimate moisture and near-surface temperature, with smaller-than-observed variability in thermodynamic environmental favorability. Together, these results suggest that the weather forecast model used here may be useful for improving forecasts of supercell environments in landfalling TCs.

1. Introduction

Tornadoes in landfalling tropical cyclones (TCs) are responsible for 3% of TC fatalities, and, at times, >$100 million dollars of damage (in 2005 dollars) that can compound the risk associated with other hazards (Rappaport, 2014; C. J. Schultz et al., 2009). However, forecasts of TC tornadoes tend to be less skillful at all lead times compared to non-TC tornadoes due in part to the large variability in the number of tornadoes spawned among TCs (Carroll-Smith et al., 2023; Edwards, 2012). Tornado warning skill is also lower in TCs compared to all environments, as evidenced by false alarm ratios of 0.86 for TC tornadoes compared to 0.70 for all tornadoes (Martinaitis, 2017; Nowotarski et al., 2021). This decreased forecast skill is likely due, in part, to differences with Great Plains tornadoes including: (a) the low CAPE, high vertical wind shear environments in TCs (McCaul, 1991; McCaul & Weisman, 1996) and (b) nearly 88% of tornadoes spawned by supercells, which are often low topped (Edwards et al., 2012; McCaul & Weisman, 1996). Specifically, these low-topped supercells are smaller, shorter-lived, and shallower than their Great Plains counterparts and, most importantly, typically spawn tornadoes with light-to-moderate damage (i.e., Enhanced Fujita (EF) or Fujita (F) scale rating of 0–1; McCaul & Weisman, 1996; L. A. Schultz & Cecil, 2009). Moreover, these TC supercells are often characterized by weaker rotational velocity and reflectivity, shallower updrafts, and, more broadly, the absence of radar characteristics typical of non-TC supercells (e.g., hook echoes; Devanas et al., 2008; Nowotarski et al., 2021). These low-topped supercells are also typically not associated with lightning before tornadogenesis, which likely limits the utility of lightning jump algorithms for tornadic detection (Schenkel et al., 2023; C. J. Schultz et al., 2009). Given the limited utility of radar and lightning data for TC tornado forecasting, recent case studies have shown promise in using convection-allowing ensembles to help identify TC tornadic mesocyclones at lead times of up to 2 hr (T. A. Jones et al., 2019; Y. Wang et al., 2022). As a more modest goal, prior work has yet to systematically evaluate whether convection-allowing models can reasonably forecast convective-scale environments in landfalling TCs, which is the focus of the present study.

The low CAPE, high vertical wind shear environments in landfalling TCs are broadly favorable for tornadoes, primarily within the right-front quadrant relative to TC motion or northeast quadrant (Baker et al., 2009; McCaul, 1991). Compared to non-TC thermodynamic environments, CAPE is often smaller and concentrated in the lower troposphere, in association with the approximately moist adiabatic lapse rates typical of TCs (Edwards & Thompson, 2012; McCaul, 1991). Prior work has also hypothesized that narrow regions of locally enhanced CAPE and helicity may exist downstream (i.e., relative to the lower-tropospheric cyclonic flow) of TC rainbands. These locally favorable environments for tornadoes may not be well-resolved within prior radiosonde climatologies (Edwards & Pietrycha, 2006; McCaul et al., 2004). However, CAPE does increase with increasing distance from the TC center (Bogner et al., 2000; Molinari et al., 2012) due to: (a) more sparse convection and associated cirrus allowing for enhanced diurnal variability of surface heating (Knupp et al., 2006; Morin & Parker, 2011) and (b) more frequent intrusions of ambient midtropospheric dry air, which may enhance lapse rates via evaporative cooling, generate baroclinicity at outer radii, or even reduce CAPE due to entrainment mixing (Curtis, 2004; Sueki & Niino, 2016). Consistent with the former hypothesis, most tornadoes, especially at TC outer radii, occur from late morning through early evening, suggesting the strong impact of diurnal heating (McCaul, 1991; Trier et al., 2023).

Favorable convective-scale kinematic environments for tornadoes are associated with strong speed and directional shear in the boundary layer due to friction, and the veering and weakening of the winds above this layer in association with the TC warm core (McCaul, 1991; Novlan & Gray, 1974). This vertical wind shear may be further enhanced by stronger friction over land as supercells move from ocean to land, providing additional horizontal vorticity to be tilted and stretched by updrafts. This horizontal gradient in friction likely explains the near-shore maximum in TC tornadogenesis (Eastin & Link, 2009; Gentry, 1983). TCs, especially those recurving into the midlatitudes, are often embedded in warm air-advection regimes upstream of ridges. The veering in the synoptic-scale environment of the TC yields enhanced vertical wind shear of the total wind field (i.e., TC plus its environment), typically on the eastern half of the TC (McCaul, 1991; Verbout et al., 2007). This asymmetric enhancement of vertical wind shear associated with the total wind field is due to: (a) constructive enhancement of veering and speed shear associated with both the TC and ambient winds and (b) the tilting of the TC with height due to differential advection by the ambient flow. The latter of these processes yields stronger lower-tropospheric inflow, ascent, upper-tropospheric outflow as a quasi-geostrophic response to the vertical tilting of the TC (Schenkel et al., 2020, 2021).

While convective-scale lower-tropospheric vertical wind shear in the TC is strongest near the center, most tornadoes occur in the outer rainbands between a 100–500 km radius in the northeast quadrant of the TC where CAPE (especially entrainment CAPE) is stronger whereas shear is reduced (Franklin et al., 2003; Sueki & Niino, 2016). Rainbands at these distances are typically associated with locally enhanced vertical wind shear due to a lower-tropospheric, TC-relative tangential jet that runs along the rainband (Barnes et al., 1983; Didlake & Houze, 2009). This localized vertical wind shear may be further enhanced by the occurrence of cold pools when ambient air is sufficiently dry (Ditchek et al., 2020; Eastin et al., 2012). The weaker TC outer winds can also be frontogenetic, enhancing baroclinicity and lift associated with pre-existing baroclinic boundaries (e.g., coastal fronts; Green et al., 2011; Knupp et al., 2006).

Skillful forecasts of TC tornadoes likely require reasonable representation of the aforementioned scales including the supercell, rainbands, TC, and its synoptic-scale environment. One model capable of simulating these scale interactions is the Warn-on-Forecast System (WoFS), which is a convection-allowing ensemble under development for use in operations, that has shown skill in simulating tornadic mesocyclones and their environments. Specifically, WoFS is a regional ensemble modeling system for use in 0–6-hr forecasts of high-impact severe convective weather, including TC tornadic supercells. Specifically, these studies have shown that WoFS can: (a) predict the life cycle and location of strongly rotating mesocyclones for a variety of severe convective weather scenarios including supercells and bow echoes (Skinner et al., 2018; Wheatley et al., 2015) and (b) represent convective-scale severe weather environments with reasonable fidelity (Laser et al., 2022; Potvin et al., 2020). More broadly, WoFS has also shown skill in forecasting other hazards including flash flooding (Lawson et al., 2018; Yussouf et al., 2016).

Nonetheless, only a few studies have evaluated the forecast skill of WoFS for TC tornadoes and their environments. Yussouf et al. (2020) showed that WoFS simulations of Hurricanes Harvey (2017), Florence (2018), and Michael (2018) reasonably represented the location of lower-tropospheric relative vorticity maxima compared to tornado reports, while also simulating the intensity and structure of heavy rainfall. A second study showed that WoFS forecasts of Hurricanes Harvey (2017) and Irma (2017) adequately forecast the location and timing of lower-tropospheric mesocyclones compared to tornado reports. These forecasts also were skillful in representing strong surface wind gusts and heavy rainfall (T. A. Jones et al., 2019). Y. Wang et al. (2022) also examined whether further improvements in WoFS simulations of Hurricanes Harvey (2017) and Michael (2018) occur by reducing the model horizontal grid spacing from 3 to 1 km. While these finer horizontal grid spacing simulations showed both stronger mesocyclone surrogates and heavier rainfall, only selected simulation cases with 1-km grid spacing showed improvements in the location and timing of mesocyclones.

Despite the promise of WoFS in simulating TC tornadic mesocyclones, no study has analyzed model skill in forecasting convective-scale environments in landfalling TCs. Knowledge of the fidelity of convective-scale environments in TCs that are favorable and unfavorable for tornadoes is key to understanding potential model biases and uncertainty, which is important for: (a) future studies identifying the environmental factors contributing to the formation and intensification of tornadic mesocyclones, (b) improving short-fused forecasts of TC tornadoes when WoFS is introduced into operations (Edwards et al., 2012; Y. Wang et al., 2022), and (c) identifying future areas of focus for development for WoFS and other convection-allowing models. Hence, this study will assess the fidelity of convective-scale environments in landfalling TCs as forecast by the WoFS system. Specifically, we will compare WoFS forecasts against National Weather Service (NWS) weather Forecast Office (WFO) and National Severe Storms Laboratory (NSSL) radiosondes, from selected landfalling hurricanes from 2020. This study is a preliminary investigation of WoFS performance due to the small sample of TCs examined, although the sample is likely large enough to only yield quantitative, rather than qualitative, changes in the conclusions if a larger, multi-year sample size were used. These soundings are not TC tornado proximity soundings, since ≈1% of radiosondes meet the proximity sounding criteria due to the short life span of tornadoes (i.e., 3-min median lifetime) and the compound hazards posed by TCs (Potvin & Flora, 2015; Schenkel et al., 2023). Rather, the soundings are used to more broadly assess the fidelity of convective-scale environments in multiple TCs. We will focus on examining TC convective-scale kinematic and thermodynamic structure and associated severe weather metrics. This study will address the following questions:

- Is WoFS able to reasonably forecast convective-scale kinematic and thermodynamic environments in TCs?
- Does the fidelity of kinematic and thermodynamic convective-scale environments substantially degrade with increasing forecast lead time?

2. Data and Methods

2.1. TC Track Data

National Hurricane Center (NHC) 6-hr TC track and intensity data for selected 2020 landfalling TCs are obtained from the International Best Track Archive for Climate Stewardships version 4, revision 0 (IBTrACS; Knapp et al., 2010). Specifically, our study only considers seven TCs whose landfall was simulated in real-time by WoFS with ≥1 radiosonde launched during the forecast period. Only radiosondes launched during the tropical phase of the TC life cycle are considered (i.e., tropical depression or stronger). These TC data are also used to help identify the model TC center and compute the TC-relative location of radiosondes.

Table 1
The Name of Each TC, its Associated Radiosondes, the Number of Forecast Soundings, and the Number of WoFS Ensemble Forecast Soundings (i.e., Number of Forecast Soundings Multiplied by 18 WoFS Ensemble Members) in This Study

TC name	Number of unique radiosondes	Number of forecast soundings	Number of WoFS ensemble forecast soundings
Tropical Storm Fay (2020)	8	56	1,008
Hurricane Hanna (2020)	8	34	612
Hurricane Isaias (2020)	20	86	1,548
Hurricane Laura (2020)	19	71	1,278
Hurricane Marco (2020)	6	6	108
Hurricane Sally (2020)	27	128	2,304
Hurricane Delta (2020)	9	38	684
All storms ($N = 7$)	97	419	7,542

Note. The Hurricane Laura (2020) radiosondes include those from the NWS and NSSL.

2.2. Radiosonde Data

Convective-scale environments with varying environmental favorability for tornadoes in TCs from WoFS are examined using radiosondes from two sources: (a) NWS WFO soundings cataloged in the National Oceanographic and Atmospheric Administration (NOAA) Integrated Radiosonde Archive (IGRA), version 2 (Durre et al., 2006) and (b) NSSL-sponsored sampling of recent landfalling TCs (Waugh, 2024). For the IGRA data, all radiosondes within 750 km of the TC center are selected for study, which is the distance over which 99% of tornadoes occur (Schenkel et al., 2020, 2021). Each radiosonde is tested for both physical and internal consistency. IGRA radiosondes are compared to model soundings from 1 hr prior for consistency with the actual radiosonde release time by NWS forecast offices (Coniglio et al., 2013). NSSL radiosondes sample Hurricane Laura (2020) with locations that were not collocated with NWS sounding sites. These NSSL soundings are processed using National Center for Atmospheric Research (NCAR) Atmospheric Sounding Processing Environment (ASPEN) software (Stern et al., 2016; J. Wang et al., 2015).

In addition to the numerous automated quality control checks in ASPEN, we have manually inspected each radiosonde. We also employ the following criteria for all radiosondes (Molinari & Vollaro, 2008; Schenkel et al., 2020): (a) data must be present below 3 km, given the importance of lower-tropospheric convective-scale environments to miniature supercells (McCaul, 1991; McCaul & Weisman, 1996) and (b) launch locations must be ≥75 km from the TC center to represent quasi-vertical profiles, since the strong cyclonic advection by the TC winds inwards of this distance. Since geolocation data are unavailable after NWS radiosonde launch, we assume that both NWS and NSSL sondes do not move horizontally above the surface. This ensures consistent treatment between the two data sets. While this assumption introduces uncertainty into our analysis, we believe there are three reasons why these errors are likely small: (a) exclusion of radiosondes within 75 km of the TC center removes those data that are advected rapidly by the TC, (b) TC supercells, which are often low-topped, are more sensitive to winds, temperature, and moisture within 3 km of the surface (Edwards et al., 2012; Morotomi et al., 2020), with any sonde drift being small over this layer, (c) prior studies of mesoscale forecast model output, including in TCs, have not corrected for radiosonde drift (Bray et al., 2021; MacDonald & Nowotarski, 2023).

These criteria yield a total of 97 radiosondes in seven landfalling TCs, with 92 NWS radiosondes from the IGRA archive and five NSSL radiosondes. These radiosondes provided comparison against 419 WoFS forecast soundings listed in Table 1, with the locations of NSSL and NWS radiosondes given in Figure 1. For each of the 419 soundings, 18 WoFS ensemble members are available for analysis against the radiosondes yielding a total of 7542 WoFS ensemble forecast soundings. All 97 soundings, and their respective 419 forecast radiosonde and 7542 WoFS ensemble soundings, are used in the composite analysis to follow, while a subset of four soundings (i.e., two NSSL and two NWS) are used in a case study of Hurricane Laura (2020) in the final results section. A single sounding may be compared to multiple forecast soundings, given that forecasts are initialized every hour. Hence, the number of forecast soundings will exceed the number of radiosondes. Most of the soundings are clustered in Gulf Coast states, due to the numerous TC landfalls during the 2020 season. The NSSL radiosondes included in this study were launched from southern Louisiana during Hurricane Laura (2020), as denoted by the

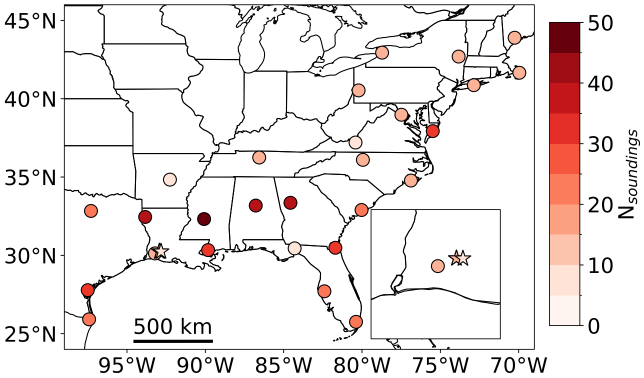

Figure 1. Map view of the WoFS forecast sounding locations in this study, with circles and starts showing the location of the National Weather Service (NWS) and National Severe Storms Laboratory (NSSL) radiosondes, respectively. The inset shows the border of Texas and Louisiana, where the NSSL radiosondes were launched near the NWS Lake Charles Weather Forecast Office.

stars in Figure 1. We only include radiosondes if the model TC location and the TC-relative radiosonde location fall within the model domain. We also show the TC-relative location of observed soundings in Figure 2. Although the soundings sample all TC-relative quadrants, approximately 43% sample the northeast quadrant, where most tornadoes occur (McCaul, 1991; Novlan & Gray, 1974).

Our analysis will compare the vertical profiles of kinematic and thermodynamic variables between the radiosondes and WoFS. To help isolate the TC winds, TC motion has been subtracted from the zonal and meridional winds for each radiosonde, using the IBTrACS computed propagation speed for the observed radiosondes and forecast TC propagation speed of each ensemble member for the WoFS soundings (Baker et al., 2009; Schenkel et al., 2021). The resulting wind field with TC motion removed is used to calculate all severe convective weather parameters listed below, including Bunkers motion, and the TC-relative tangential and radial winds. However, subtracting a uniform wind speed and/or direction from the entire wind profile is not an option in the software (e.g., AWIPS) used by operational forecasters. We will also use several lower-tropospheric severe convective weather metrics including 0–3-km convective available potential energy (CAPE), 0–500-m storm-relative helicity (SRH), and 0–3-km SRH (Davies-Jones, 1984), in addition to mixed-layer CAPE. Recent prior work has suggested that the 0–500-m layer above ground level is important for tornadogenesis, which is likely particularly true for TC supercells due to their shallow depth (Coffer et al., 2019; Morotomi et al., 2020), which motivates the use of 0–500-m SRH in the present study.

Our study has six vertical levels within the lowest 500 m, which is the same number as the Coffer et al. (2019) study. The "storm" in SRH refers to convective cells, rather than TCs and the associated ambient, synoptic-scale vertical wind shear (Onderlinde & Nolan, 2014; Schenkel et al., 2020). For all CAPE calculations, we used a 200-m mixed layer similar to prior TC studies (Molinari et al., 2012; Schenkel et al., 2020). Lower-tropospheric metrics are primarily examined, given that favorable environments for tornadoes are present over a shallower layer compared to non-TC environments (McCaul, 1991; McCaul & Weisman, 1996).

When calculating SRH, cell motion is computed using the layer between the lifting condensation level and 65% of the equilibrium level, which performs better for shallow supercells compared to the Bunkers et al. (2000) algorithm (Bunkers et al., 2014). This modified Bunkers motion algorithm can be sensitive to small changes in winds with height (Coniglio & Parker, 2020), which is a source of uncertainty. Our helicity values may be overestimated by 5%–8% due to the strong cyclonic curvature of the TC winds as the radiosondes are rapidly advected cyclonically (Molinari & Vollaro, 2010). Before computing these parameters, we also coarsen the observed radiosonde data to the model output grid (Coniglio, 2012; Laser et al., 2022). Following the prior convention, we use TC-relative tangential and radial winds, rather than zonal and meridional winds, to understand how deficiencies in the representation of the TC winds and its associated vertical wind shear contribute to forecast error and uncertainty (Baker et al., 2009; McCaul, 1991).

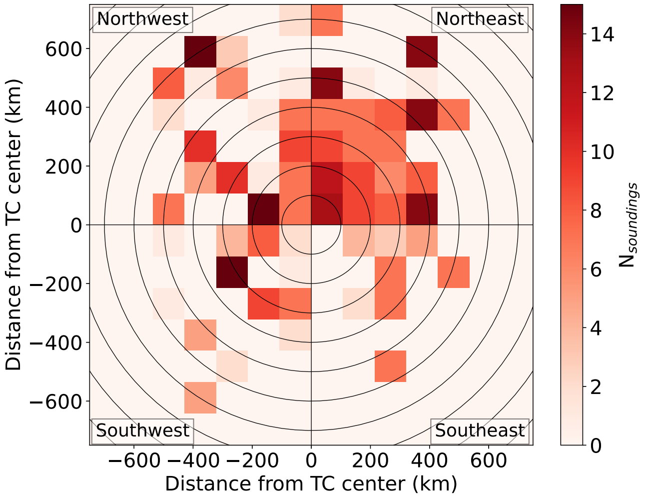

Figure 2. Joint histogram of the tropical cyclone (TC)-relative distance (km) of WoFS forecast soundings from the TC. The azimuthal coordinate is relative to the North, which is on the top of the plot. Range rings are drawn every 100 km.

2.3. WoFS Configuration

WoFS is a state-of-the-art, frequent-update cycle multiphysics regional ensemble system being developed for operations (T. A. Jones et al., 2016; Skinner et al., 2018). The 2020 version of WoFS uses a custom version of the Advanced Research Weather Research and Forecasting model (WRF-ARW version 3.9.1; Developmental Testbed Center, 2008) together with an Ensemble Kalman filter (EnKF; Houtekamer et al., 2005; Whitaker et al., 2008) from the Community Gridpoint Statistical Interpolation (GSI-EnKF; Kleist et al., 2009). The current configuration of WoFS in this study

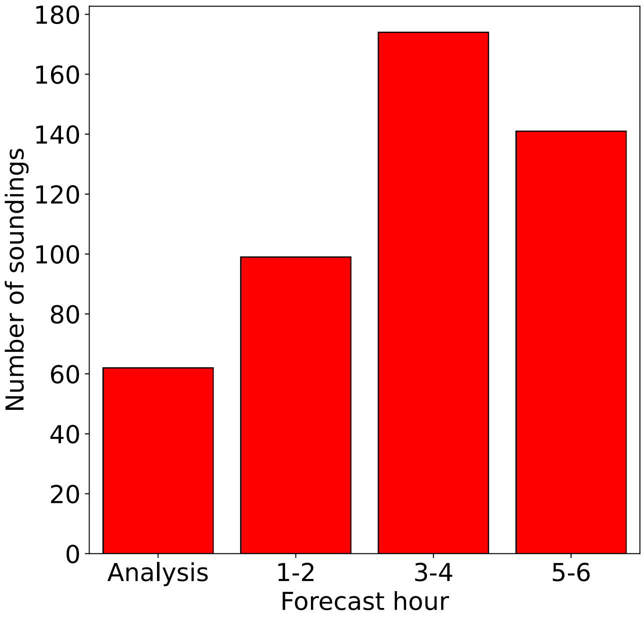

Figure 3. Histogram of WoFS sounding forecast hour in this study.

uses 18 ensemble members with a 3-km horizontal grid spacing, containing 300 × 300 grid points with 51 hybrid sigma-pressure vertical levels, using a vertical grid spacing of $\leq$100 m near the surface that decreases to $\geq$1 km at the model top (Wheatley et al., 2015; Yussouf et al., 2020). Each ensemble member uses initial and boundary conditions from 1-hr experimental, 18-member High-Resolution Rapid Refresh Ensemble forecasts (HRRRE; Dowell et al., 2016). All ensemble members use the NSSL 2-moment microphysics parameterization (Mansell et al., 2010) and the Rapid Refresh land-surface scheme (Benjamin et al., 2016). The 18-member WoFS ensemble is generated from the use of a unique HRRRE ensemble member for each WoFS ensemble member, together with added physics diversity through differing combinations of radiation and planetary boundary layer parameterizations. Specifically, the radiation parameterization combinations used include the: (a) Rapid Radiative Transfer Model shortwave (Mlawer et al., 1997) and Dudhia longwave scheme (Dudhia, 1989) and (b) Rapid Radiative Transfer Model-Global shortwave and longwave schemes (Iacono et al., 2008). Planetary boundary layer parameterization schemes chosen include the: (a) Yonsei University (Hong et al., 2006), (b) Mellor-Yamada-Janjic (Janjić, 1994), and (c) Mellor-Yamada-Nakanishi-Niino schemes (Nakanishi & Niino, 2004).

Real-time 6-hr WoFS forecasts were initialized every hour beginning in the afternoon and evening of the TC landfall day, which approximately overlaps with the peak diurnal frequency of tornadoes (McCaul, 1991; L. A. Schultz & Cecil, 2009). A 15-min cycling frequency is used to assimilate hourly Automated Surface Observing Systems (ASOS) and Oklahoma Mesonet data (for cases when the model grid extends over Oklahoma), Weather Survellience Radar-1988 Doppler (WSR-88D) reflectivity and velocity data, and Geostationary Operational Environmental Satellite-16 (GOES-16) satellite cloud water path observations. NWS and NSSL radiosondes in selected landfalling TCs are not assimilated by WoFS nor in the HRRRE forecasts, since these data are not available for assimilation into the analysis. Hence, these soundings provide an independent data source for model validation.

We show a histogram of forecast hours for each of the forecast soundings that the radiosondes are compared against in Figure 3, due to the focus on forecast performance as a function of lead time. The number of soundings is generally skewed toward later forecast hours. We also show the launch time of all radiosondes in Figure 4, where NWS radiosondes are assumed to be launched 1 hr before synoptic times, as previously mentioned. NSSL radiosondes are launched at non-synoptic times from locations that are not collocated with NWS offices as shown in Figure 1.

2.4. TC Center Tracking

We employ an object-based algorithm that uses a spatially smoothed geopotential centroid to compute WoFS soundings in a TC-relative framework for each ensemble member for a given forecast. This methodology is similar to previously employed algorithms used to study both precipitation features and TCs (Davis et al., 2006; Rios-Berrios et al., 2018). Prior work has recommended the use of a centroid, similar to our approach, to avoid sharp changes in TC track associated with local extrema (Nguyen et al., 2014; Ryglicki & Hart, 2015). This methodology is applied to 850-hPa geopotential height, which is interpolated from the model output grid to 850 hPa using logarithmic interpolation. Prior work has used the 850-hPa isobaric level, or similar, to define the TC center location for cases undergoing moderate vertical wind shear (Rios-Berrios & Torn, 2017; Rios-Berrios et al., 2016). The object-oriented methodology consists of three steps (Davis et al., 2006; Rios-Berrios et al., 2018): (a) apply a nine-point smoother to the field of interest, (b) retain the top 5% of points, and (c) identify the center as the geopotential centroid computed within a 50-km radius of the first guess, which is assumed to be the observed location from IBTrACS:

$$\mathbf{x}' = \frac{\int_x \int_y \Lambda \mathbf{x} dxdy}{\int_x \int_y \Lambda dxdy} \tag{1}$$

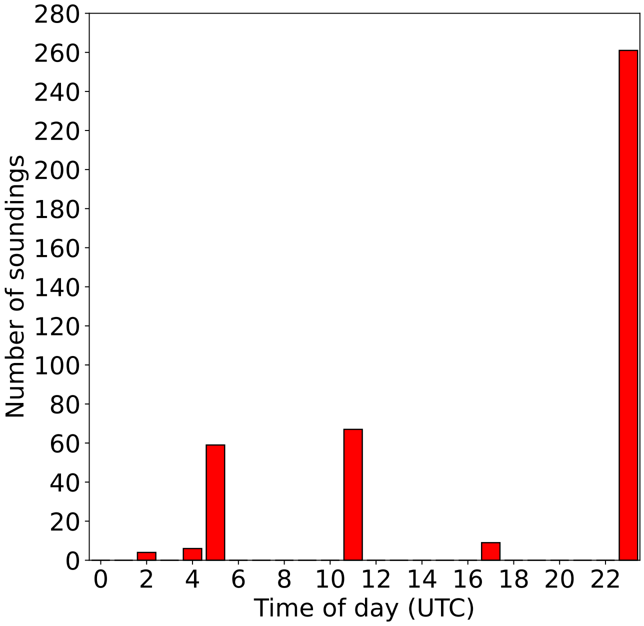

Figure 4. Histogram of WoFS sounding launch time (UTC) in this study. National Weather Service radiosondes are assumed launched 1 hr before synoptic times, while National Severe Storms Laboratory radiosondes are launched at non-synoptic times.

where $\mathbf{x}'$ is the TC center location (i.e., geopotential centroid), $\mathbf{x}$ is the position vector at each grid point, and Λ is the 850-hPa geopotential height. The centroid is iteratively computed until convergence for a particular point. The mean TC center difference between WoFS and observations is 52 km, which is comparable to the mean position uncertainty inherent to the IBTrACS data for landfalling TCs (i.e., 33 km; Landsea & Franklin, 2013). Non-trivial uncertainty in the WoFS TC center location exists, which should be considered, due to the following: (a) choice of isobaric level in vertically tilted TCs (Fischer et al., 2022; Reasor et al., 2013), (b) TC center tracking method selected (Nguyen et al., 2014; Ryglicki & Hart, 2015), and (c) uncertainty in IBTrACS TC center location (Landsea & Franklin, 2013; Torn & Snyder, 2012).

2.5. Vertical Coordinates

Vertical soundings from radiosondes and WoFS data are interpolated to the vertical coordinate of Gal-Chen and Somerville (1975) to facilitate comparison of radiosondes with different launch altitudes (Parker, 2014; Schenkel et al., 2020):

$$z^* = H\frac{z - z_{sfc}}{H - z_{sfc}} \tag{2}$$

where z_{sfc} is the radiosonde launch altitude and H is assumed to be 16 km consistent with the tropopause height in North Atlantic TCs, including those spawning tornadoes after landfall (Duran & Molinari, 2016; Waco, 1970). However, there may exist non-trivial variability in tropopause height, especially for any cases undergoing extratropical transition (Evans et al., 2017; S. C. Jones et al., 2003). There may also be uncertainty introduced in assuming the tropopause height is 16 km in both WoFS and radiosondes, although past work has not varied the tropopause height for this coordinate despite differences in synoptic environments, including for TCs (Parker, 2014; Schenkel et al., 2020). Moreover, the results to follow only show small differences in upper-tropospheric temperature (typically used in defining tropopause height) between WoFS and the radiosondes, suggesting only small differences in tropopause heights between the two data sets. Typically, the radiosonde launch altitude is within 10 m of the surface. This coordinate allows for comparison of soundings with differing launch altitudes, while approximately conserving vertically integrated quantities like CAPE and SRH. When referencing specific heights during the analysis to follow, height values near the surface are approximately equal to the height above ground level in the vertical coordinate used here. In contrast, heights approaching the 16 km tropopause used above are roughly equivalent to a height above mean sea level (Parker, 2014). To ensure the WoFS and radiosonde data match in time and space, we then: (a) coarsen the vertical resolution of the radiosonde data to the WoFS vertical grid (Coniglio, 2012; Laser et al., 2022), and (b) interpolate the WoFS data to the time and TC-relative location of the radiosonde launch location.

2.6. Statistical Testing

We employ a 10,000-sample bootstrap approach (with replacement) with a two-tailed test at the 5% level to objectively determine differences in the statistics between two distributions. We also use bootstrap resampling to calculate the 95% confidence interval of the variables being examined, and whether the Pearson correlation coefficients are statistically different from 0 at the 1% level. Specifically, our study will use the bootstrap approach to test differences among the kinematic and thermodynamic structure of the convective-scale environments in TCs, and their associated severe weather metrics. Our study assumes that the degrees of freedom are equal to the number of forecast soundings.

3. Analysis and Results

Section 3.1 will assess the fidelity of convective-scale kinematic environments in TCs. Following this, Section 3.2 will examine the representation of convective-scale thermodynamic environments. Finally, Section 3.3 discusses

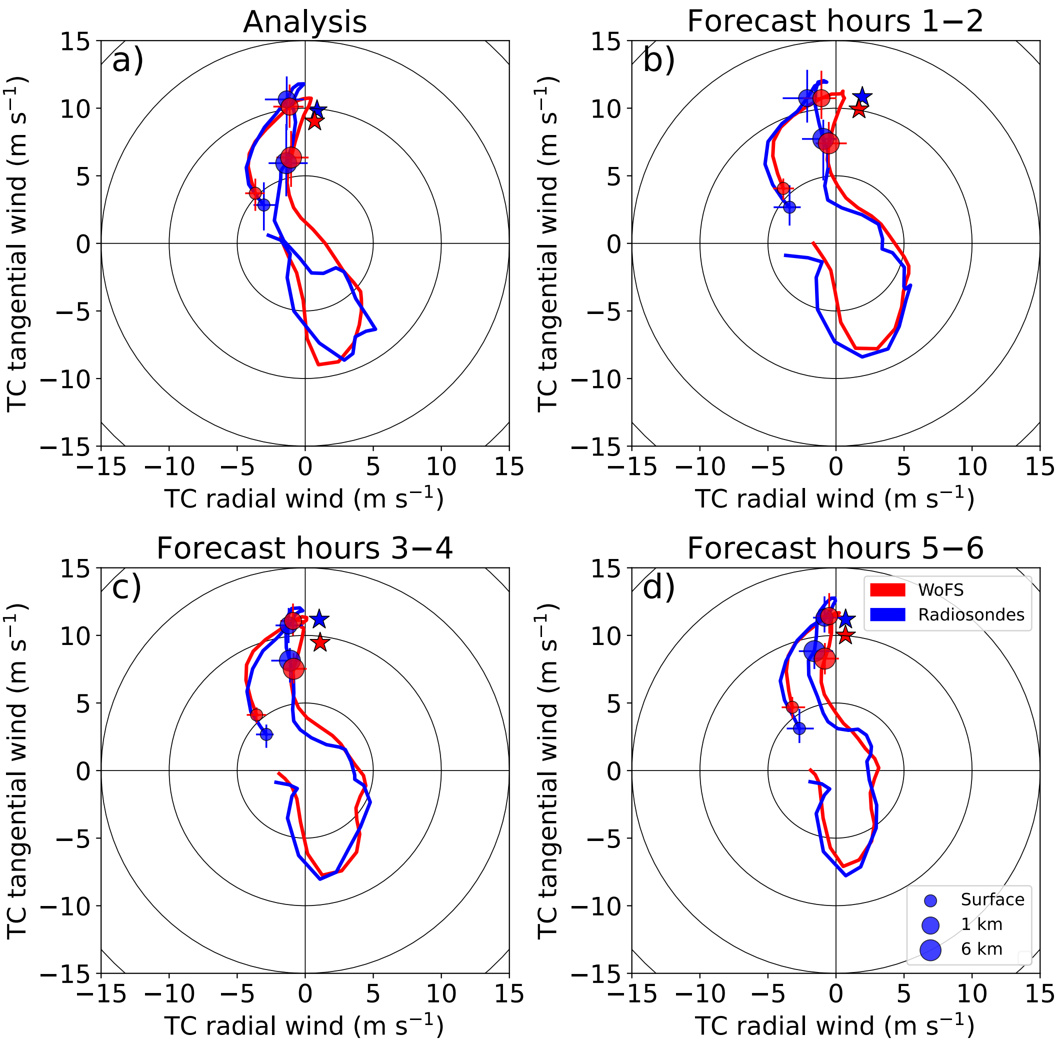

Figure 5. Composite median hodographs of the tropical cyclone (TC)-relative radial wind (m s^{-1}) versus TC-relative tangential wind (m s^{-1}) computed for observed and WoFS soundings for the (a) analysis, (b) forecast hours 1–2, (c) forecast hours 3–4, and (d) forecast hours 5–6. The star shows the median cell motion computed using a modified Bunkers storm motion algorithm (Bunkers et al., 2014). Winds at the surface, 1 km, and 6 km are shown by dots, with error bars denoting the 95% confidence interval at each level, quantified using a 10,000-sample bootstrap approach with replacement. Range rings are shown for every 5 m s^{-1}. Each hodograph has been smoothed in the vertical dimension with a 1-2-1 smoother. TC motion has been removed from each hodograph to help isolate the TC winds following Baker et al. (2009).

a case study of four selected soundings (i.e., two NWS and two NSSL radiosondes) from Hurricane Laura (2020), which was well-sampled by radiosondes.

3.1. Kinematic Environments

We first examine composite median hodographs as a function of forecast hour in Figure 5, using TC-relative radial versus tangential winds. This reference frame helps identify the contribution of the TC wind field to forecast errors in convective-scale vertical wind shear (Baker et al., 2009; McCaul, 1991). Both observed and WoFS hodographs at all forecast hours show the following characteristics similar to prior observational studies (McCaul, 1991; Schenkel et al., 2020): (a) strong speed and directional shear in the boundary layer (i.e., lowest ≈1 km) due to decreasing impacts of friction with height and (b) veering and weakening of the winds above this layer associated with the TC warm-core structure. The broad depth of the tangential wind maximum between 1 and 6 km shown in the radiosondes and WoFS is consistent with the vertical structure of the along-TC rainband tangential jet, which tends to be associated with a weaker, deeper, and more elevated wind maximum compared to

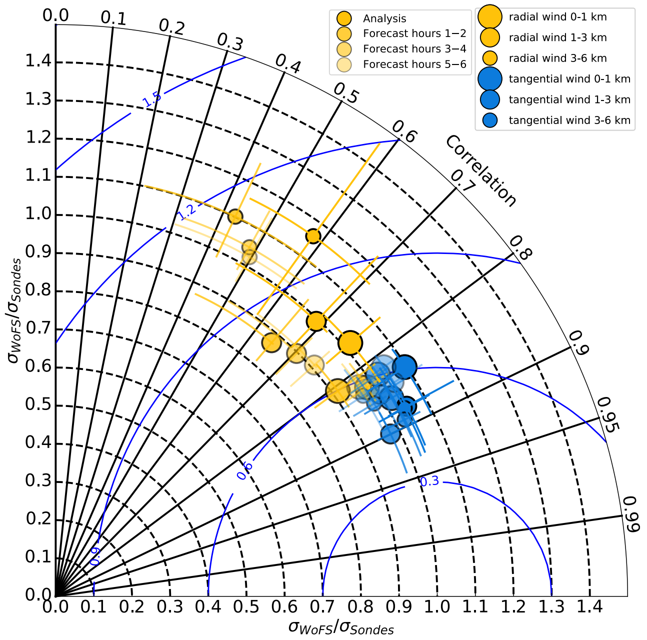

Figure 6. Taylor diagram showing Pearson correlation coefficients (black solid lines), normalized standard deviations (black dashed lines), and root-mean-square difference (solid blue lines) of tropical cyclone-relative radial (m s^{-1}) and tangential wind (m s^{-1}) between radiosondes and WoFS soundings for the analysis, forecast hours 1–2, forecast hours 3–4, and forecast hours 5–6 for the 0–1-km, 1–3-km, and 3–6-km vertical layers. Error bars show the 95% confidence interval calculated using a 10,000-sample bootstrap approach with replacement.

the eyewall (Franklin et al., 2003; Hence & Houze, 2008). Small, non-significant differences (at the 5% level) exist according to testing of data, in the lowest 3 km above the surface, at selected heights shown in Figure 5 between the observed and WoFS soundings. This lower layer is particularly important to low-topped TC supercells (McCaul & Weisman, 1996; Morotomi et al., 2020). Specifically, median differences among the hodographs within the 0–3-km layer range between −1.9–1.0 m s^{-1} for radial winds and −2.0–1.1 m s^{-1} for tangential winds. These values are on the order of the uncertainty associated with radiosonde wind measurements (i.e., ≈2.0 m s^{-1}; Dawson et al., 2012; Durre et al., 2006). These differences show small, non-significant, at the 5% level, increases in magnitude with forecast lead time, for both median radial and tangential winds.

Taylor diagrams of radiosonde versus WoFS TC-relative tangential and radial winds, as a function of forecast hour and tropospheric layer, are used to quantify the accuracy and variability of the TC winds (Figure 6). WoFS tangential winds more strongly match observations relative to the radial winds as shown by a comparison of correlations for all forecast hours and vertical layers (R = 0.82–0.90 for tangential winds vs. R = 0.43–0.83 for radial winds). The variability of tangential winds in WoFS is also more consistent with observations ($\sigma_{WoFS}/\sigma_{sondes}$ = 0.96–1.09) relative to radial winds ($\sigma_{WoFS}/\sigma_{sondes}$ = 0.87–1.16), as shown by the tighter clustering around 1.00. The strongest differences between the tangential and radial winds occur in the 3–6-km layer and, to a lesser extent, the 1–3-km layer as seen by significant differences at the 5% level in both the correlation and normalized standard deviations. These results may be partially associated with the stronger sensitivity of the radial winds to the accuracy of the TC center location (Nguyen et al., 2014; Ryglicki & Hart, 2015). Unlike the tangential winds, the fidelity of the radial winds degrades with height for all forecast hours. This is supported by a significant decrease in correlations and a significant increase, both at the 5% level, in normalized standard deviation in the 3–6-km layer (R = 0.43–0.58; $\sigma_{WoFS}/\sigma_{sondes}$ = 1.02–1.16), compared to the 0–1-km layer (R = 0.76–0.83; $\sigma_{WoFS}/\sigma_{sondes}$ = 0.91–1.02). The reduction in skill with increasing height above ground for radial winds may be partially attributed to the use of radar scanning strategies that increase the sampling of lower levels at the expense of upper levels in landfalling TCs, since radar data are assimilated into WoFS (i.e., Supplemental Adaptive Intra-Volume Low-Level Scan (SAILS); Chrisman, 2011). Last, no significant change in correlations or normalized standard deviations, at the 5% level, are associated with either the tangential or radial winds for increasing forecast lead time.

The distribution of differences between WoFS and radiosonde TC-relative tangential and radial winds at each vertical level are shown next in Figure 7. Calculating the distribution of differences shows biases not shown by simply showing the median of the radiosonde and WoFS distributions separately, especially when one of the distributions is more strongly skewed. Figure 7 suggests that the TC winds in the WoFS simulations are biased slightly weaker than observed, which begin in the initial forecast hours. These biases are most pronounced in the TC-relative radial winds, which are shifted toward negative values throughout most of the lower and mid-troposphere. This result suggests weaker inflow toward the TC center in WoFS as shown by comparison with Figure 5. These disparities are strong enough such that median differences, particularly below ≈10 km, are significantly different from 0 at the 5% level. Specifically, differences range between −2.1–1.1 m s^{-1} among each of the forecast hour subsets. In contrast to the prior results, these weak biases in radial winds exist over a greater tropospheric depth after the analysis. In particular, these biases manifest most strongly between ≈2 and 5 km in the analysis compared to ≈2–10 km at forecast hours 3–4.

TC-relative tangential winds (Figures 7b, 7d, 7f, and 7h) also show similar biases primarily confined to the lower troposphere: (a) stronger winds in WoFS below ≈1 km compared to radiosondes and (b) weaker winds above ≈1 km. The stronger near-surface WoFS winds are exemplified by median differences that are significantly different from 0, at the 5% level, with values ranging from −2.3–0.3 m s^{-1} among forecast hour bins. This near-surface bias may be related to the TC wind field response to surface friction, which is particularly complex

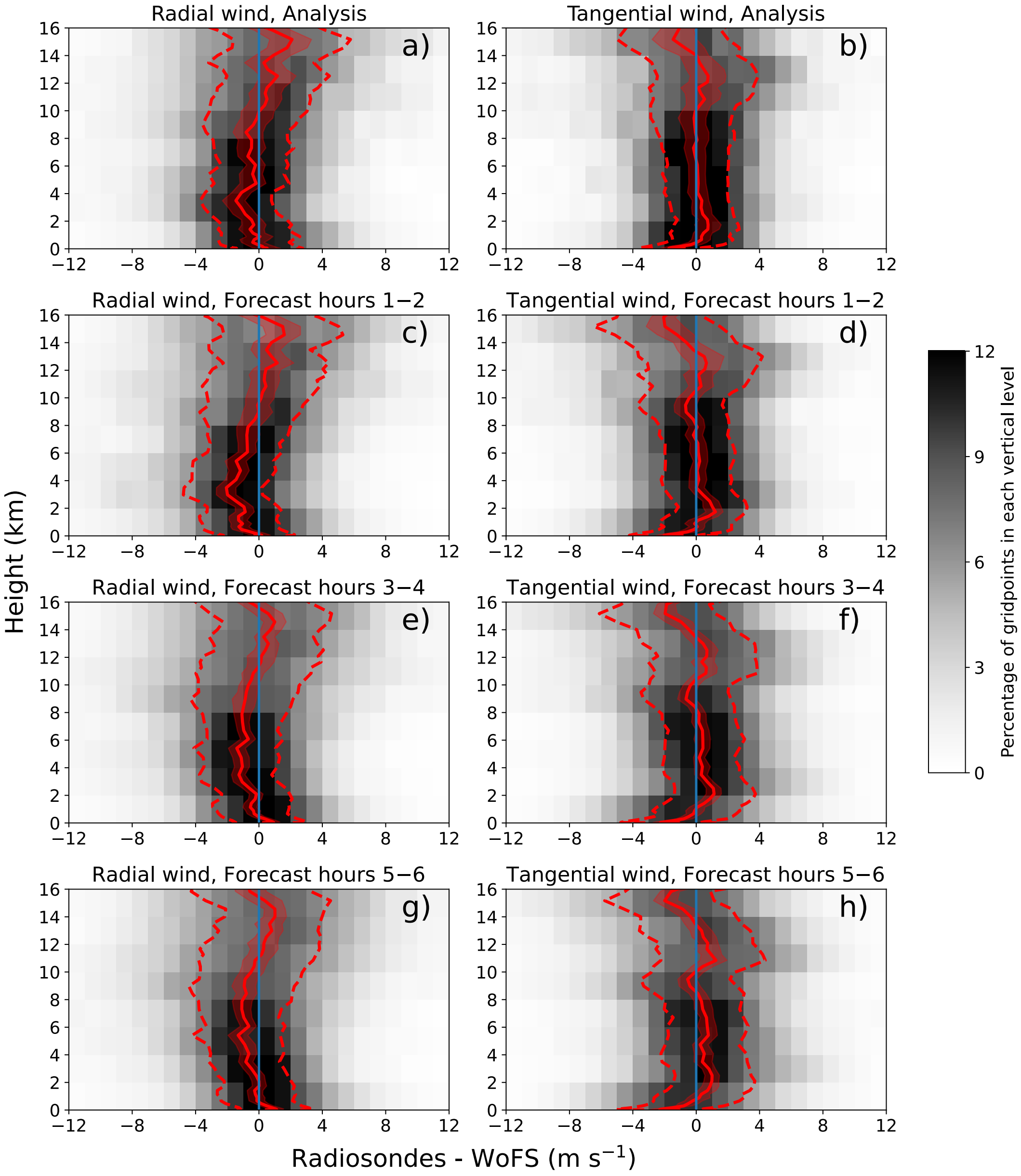

Figure 7. Joint histogram of the difference in tropical cyclone-relative (a, c, e, g) radial winds (m s^{-1}) and (b, d, f, h) tangential winds (m s^{-1}) for observed versus WoFS soundings, as a function of height (km), for the (a, b) analysis, (c, d) forecast hours 1–2, (e, f) forecast hours 3–4, and (g, h) forecast hours 5–6. The shaded boxes denote the percentage of grid points normalized by the total number of grid points for each vertical level. The median, its 95% confidence interval, and the interquartile range are shown using red solid lines, red shading, and red dashed lines, respectively.

immediately onshore in observations (Alford et al., 2020; Hlywiak & Nolan, 2022). Prior work has also shown model sensitivity of onshore TC structure to the model land use type classification and the planetary boundary layer parameterization chosen (Hendricks et al., 2021). Above the boundary layer, median values of WoFS tangential winds are significantly weaker than radiosondes (at the 5% level) with differences of 0.0–1.2 m s^{-1}. These weaker tangential winds are maximized at a 2-km height above ground level, approximately within the base of the lower-tropospheric tangential jet maximum located in the TC rainbands. These tangential wind differences are associated with a weaker wind maximum that peaks slightly higher in the troposphere in WoFS compared to observations, yielding slightly weaker than observed lower-tropospheric vertical wind shear (Didlake & Houze, 2009; Hence & Houze, 2008), as suggested by Figure 5. Like the TC-relative radial winds, the biases in the tangential winds at all levels begin to strongly manifest after the analysis time, as supported by the occurrence of median values that are significantly different from 0 at the 5% level.

Examination of 0–3-km and 0–500-m SRH from WoFS shows reasonable agreement, albeit with stronger variability, compared to observations as shown in Figure 8. For reference, the strong near-surface vertical wind shear in TCs leads to most helicity concentrated below 1 km above the surface in TCs, although the 0–3-km layer is also a useful metric for tornado forecasting (Coffer et al., 2019; McCaul, 1991). In particular, correlation coefficients range from moderate to strong with each significantly different from 0 at the 5% level for the 0–3-km ($R = 0.67$–0.88) and 0–500-m layer ($R = 0.60$–0.79), regardless of forecast hour bin. No significant variability occurs, at the 5% level, when stratifying these results by forecast hour. Reasonable agreement exists between WoFS and the radiosondes at smaller observed helicity magnitudes, with increasing underestimates as observed values increase. This result is consistent with the small linear regression coefficients that are significantly different from 1.00 for half of the forecast hour bins considered in both layers, at the 5% level. WoFS helicity values show stronger variability than the radiosondes as exemplified by comparison of the standard deviation in the 0–3-km layer (109–136 $\mathrm{m^2\ s^{-2}}$ in radiosondes vs. 126–143 $\mathrm{m^2\ s^{-2}}$ in WoFS) for data aggregated across all forecast hours, with larger differences for the 0–500-m layer (80–88 $\mathrm{m^2\ s^{-2}}$ vs. 84–119 $\mathrm{m^2\ s^{-2}}$). This larger-than-observed variability is consistent with the TC-relative radial and tangential wind results shown in Figure 6.

Of those radiosondes that exceed the 100 $\mathrm{m^{-2}\ s^{-2}}$ threshold in the 0–3-km layer associated with TC tornadoes, only 52% of the equivalent WoFS soundings also exceed this threshold, further suggesting an underestimation of large SRH values in TCs (Eastin & Link, 2009; Edwards et al., 2012). These weaker-than-observed large SRH magnitudes are broadly consistent with TC and non-TC environments both in WoFS and other convection-permitting models (Laser et al., 2022; MacDonald & Nowotarski, 2023). This bias may exist due to the weaker-than-observed TC-relative radial winds and vertical shear of the TC-relative tangential winds shown in Figure 7. Additionally, the relatively coarse vertical grid spacing in WoFS (i.e., 100 m near the surface) may also be associated with the smaller than observed values of helicity, given the strong vertical variability in TC boundary layer winds (Barnes et al., 1983; Franklin et al., 2003).

Together, these results suggest a reasonable representation of TC-relative tangential winds and, to a lesser extent, radial winds in WoFS, regardless of forecast lead time, with a slight weak bias. This may be due, in part, to the underestimation of TC intensity in WoFS (not shown), especially when the TC is offshore and out of WSR-88D radar range, since WoFS does not assimilate aircraft reconnaissance data (e.g., radar, dropsondes). However, prior work has shown that the observed winds at TC outer radii, where most radiosondes are sampling and most tornadoes occur, show a weak relationship with TC inner-core winds (Chavas & Emanuel, 2010; Merrill, 1984). Hence, these studies suggest any intensity underestimation in WoFS should have a small impact on outer TC winds. While SRH calculations from WoFS also compare well with observations, the distribution of helicity in WoFS tends to underestimate values at the upper end of the distribution. These larger values of helicity have been hypothesized to be associated with localized regions of enhanced CAPE in tornadic TC rainbands and, thus, may not be sampled by the radiosondes, as discussed previously (Green et al., 2011; McCaul et al., 2004). Therefore, these results suggest the importance of resolving these environments for forecasting tornadic supercells. Machine learning models may be able to bias correct these underestimated helicity values in WoFS to provide additional value to forecasters, especially since machine learning has already shown improved skill over raw WoFS output in non-TC scenarios (Clark & Loken, 2022; Flora et al., 2021).

3.2. Thermodynamic Environments

Composite median skew T-log$p$ diagrams show that the thermodynamic environments compare reasonably between the radiosondes and WoFS (Figure 9). Both WoFS and the radiosondes show nearly moist adiabatic lapse rates with low CAPE, relative to Great Plains tornadic supercell environments, typical of the tropical environments in TCs (McCaul, 1987, 1991). However, WoFS is biased moister and, to a lesser extent, warmer in the boundary layer. Above the boundary layer, WoFS is cooler and moister suggesting that it is closer to saturation than observations within this layer. Due to the approximately moist adiabatic lapse rates, these temperature and moisture biases are often associated with substantially larger mixed-layer CAPE in WoFS compared to observed environments where there is little to none, as will be shown later in Figure 12. However, these differences in temperature and dewpoint, especially in the lower troposphere (i.e., lowest 3 km), are small and not significant at the 5% level, at all forecast lead times throughout the troposphere. Median differences range from −0.6–0.6°C for

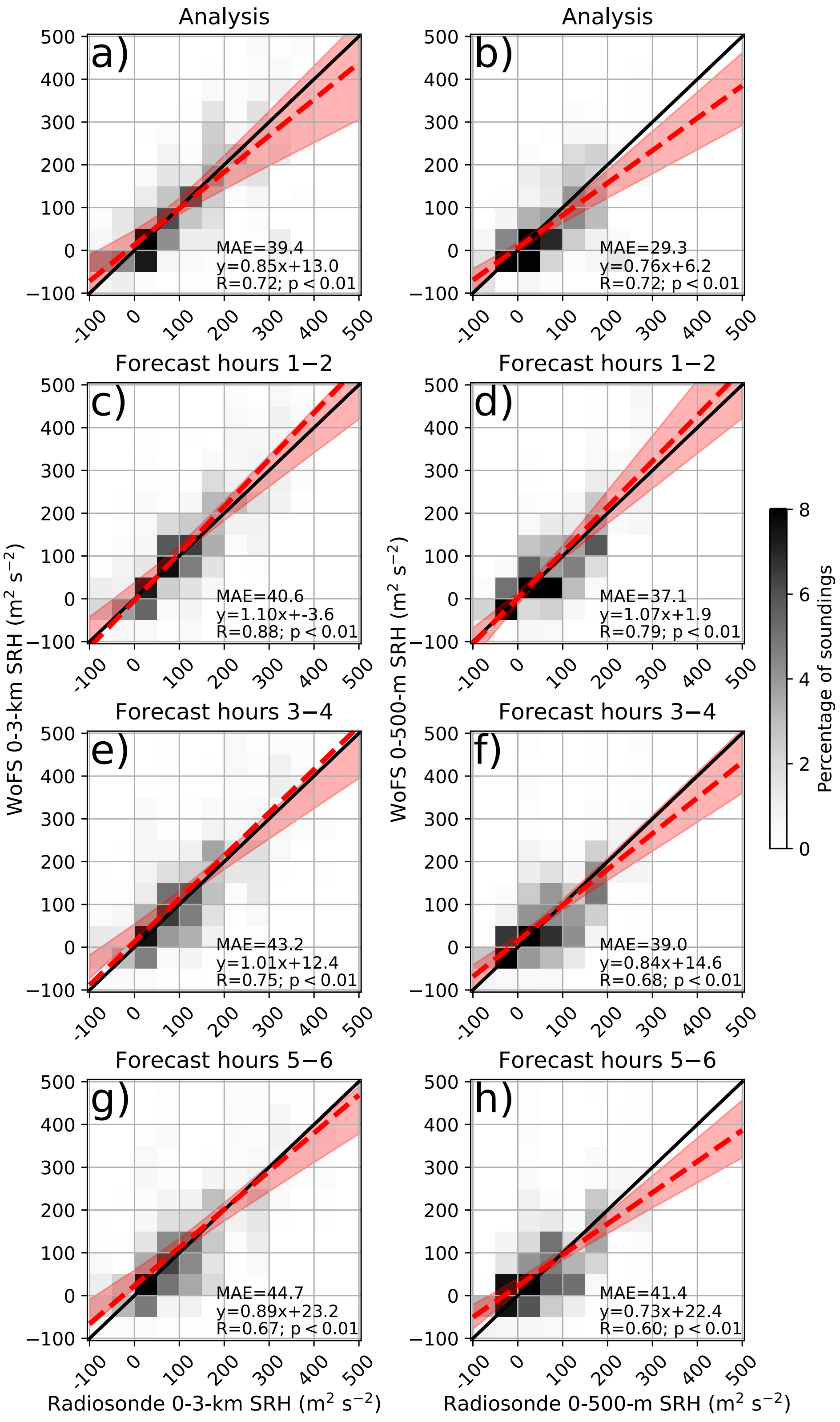

Figure 8. Joint histogram of (a, c, e, g) 0–3-km and (b, d, f, h) 0–500-m storm-relative helicity (m^2 s^{-2}) from the radiosondes versus WoFS for the (a, b) analysis, (c, d) forecast hours 1–2, (e, f) forecast hours 3–4, and (g, h) forecast hours 5–6. Median absolute error (MAE), linear regression equations, correlation coefficients, and their *p*-values are provided in each panel. The dashed red line and shading show the linear regression and its 95% confidence interval.

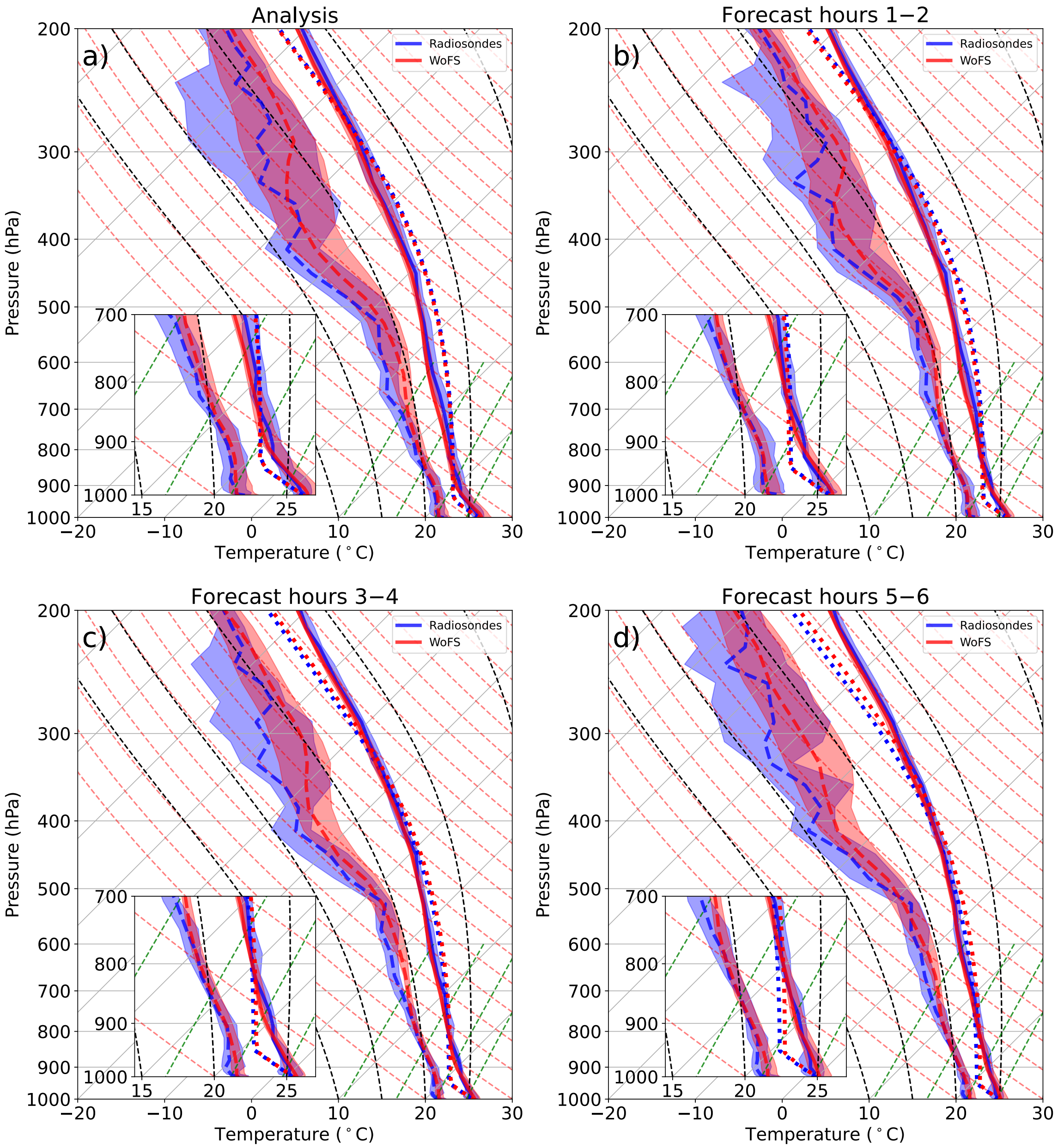

Figure 9. Skew *T*–log*p* diagram showing the composite median temperature (°C; solid lines) and dewpoint (°C; dashed lines) along with their 95% confidence interval computed from a 10,000-sample bootstrap resampling approach, with replacement (shading), for radiosonde versus WoFS soundings for the (a) analysis, (b) forecast hours 1–2, (c) forecast hours 3–4, and (d) forecast hours 5–6. The dotted lines show the theoretical median parcel ascent curve based on parcel theory.

temperature and −0.1–1.0°C for dewpoint, respectively, within the lowest 3 km. This layer is particularly relevant, given that the limited CAPE in TCs is typically concentrated in the lower troposphere, and that TC supercells can be as shallow as 3–4 km in depth (McCaul & Weisman, 1996; Morotomi et al., 2020). These values are also of comparable magnitude to the uncertainty associated with radiosonde measurements of temperature (0.2°C) and dewpoint (0.5°C; Durre et al., 2006).

We next show Taylor diagrams of temperature and dewpoint for WoFS versus observations in Figure 10. Both the correlations and normalized standard deviations suggest stronger agreement between the radiosondes and WoFS for temperature ($R = 0.88$–0.96; $\sigma_{WoFS}/\sigma_{sondes} = 0.94$–$1.00$ for all bins) compared to dewpoint ($R = 0.74$–0.86; $\sigma_{WoFS}/\sigma_{sondes} = 0.68$–$0.92$), similar to non-TC environments (Laser et al., 2022; Potvin et al., 2020). The 0–1-km layer has the strongest correlations for dewpoint ($R = 0.83$–0.86) with significant decreases in correlations as height

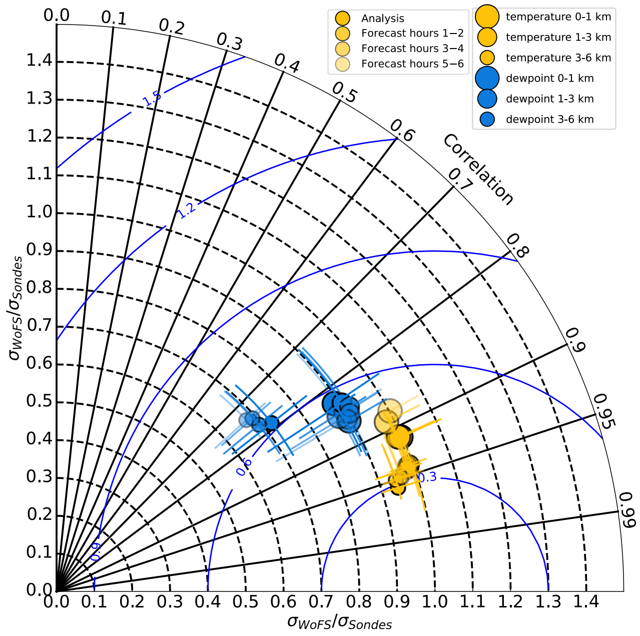

Figure 10. As in Figure 6, but for temperature (°C) and dewpoint (°C).

increases (e.g., $R = 0.74$–0.79 for 3–6-km layer), at the 5% level, also similar to these prior WoFS studies. Although the correlations remain strong, their degradation with height is likely due to a large number of in situ surface moisture observations constraining near-surface layers. Above-surface data available for assimilation are typically more sparse, especially in areas with clouds where satellite data cannot be assimilated due to its inherent uncertainty (Derber & Wu, 1998; T. A. Jones et al., 2018). In contrast, temperature shows small, yet non-significant, increases at the 5% level in the correlation between the 0–1-km layer and those layers above it. Compared to the correlations, normalized standard deviation also shows a significant reduction with height, at the 5% level, for dewpoint ($\sigma_{WoFS}/\sigma_{sondes} = 0.88$–$0.90$ for 0–1-km layer vs. $\sigma_{WoFS}/\sigma_{sondes} = 0.68$–$0.72$ for 3–6-km layer), which are larger changes than those for temperature ($\sigma_{WoFS}/\sigma_{sondes} = 0.98$–$1.00$ vs. $\sigma_{WoFS}/\sigma_{sondes} = 0.94$–$0.96$). These decreases are due to strong increases in radiosonde variability that are underestimated by WoFS. Last, neither temperature nor dewpoint show significant reductions, at the 5% level, in correlations and normalized standard deviations with increasing forecast lead time in any vertical layer.

Vertical profiles of the temperature difference between WoFS and the radiosondes show three regions with strong changes after the analysis (Figures 11a, 11c, and 11e). First, WoFS is shifted toward warmer boundary-layer temperatures, similar to biases observed in non-TC environments (Laser et al., 2022). This bias is exemplified by median differences that are significantly different from 0, at the 5% level, with magnitudes as large as 0.8°C. Above the boundary layer, WoFS is biased toward cooler than observed values, although these differences are smaller than in the boundary layer (i.e., median differences up to 0.6°C), and are not consistently present. These cooler temperatures together with the warmer than observed temperatures in the boundary layer suggest slightly steeper than observed lapse rates in WoFS. WoFS is also shifted toward warmer temperatures than observed above 14 km as shown by significant, yet small median differences, at the 5% level, ranging from −0.9 to 0.2°C. The height of these erroneous differences is maximized at ≥16 km, which may be attributed to displacements in the height of upper-tropospheric warm temperature anomalies associated with the TC warm core (i.e., observed maximum at 14 km), the tropopause (i.e., observed height of 15–17 km), or the overlying stratospheric cool temperature anomalies (Frank, 1977; Stern & Nolan, 2012).

Figures 11b, 11d, and 11f show that WoFS is biased moister particularly within the mid and upper troposphere, with these biases occurring both in the analysis and all forecast lead times. The moister than observed troposphere in WoFS is sufficiently large to be associated with medians that are significantly greater than 0 at the 5% level, with values ranging from −4.4 to 0.0°C. These differences occur throughout most of the troposphere and typically increase with height such that maximum differences are located at 16 km. A similar bias has been observed in non-TC environments in WoFS, as well as in TC environments in other convection-allowing models (e.g., High-Resolution Rapid Refresh; Laser et al., 2022; MacDonald & Nowotarski, 2023).

Both 0–3-km CAPE and mixed-layer CAPE are reasonably represented in WoFS, albeit with a narrower distribution compared to observations (Figure 12). Relative to Great Plains environments, CAPE is weaker in TCs while being primarily confined to the lower troposphere (McCaul, 1991; Schenkel et al., 2020). Both 0–3-km CAPE ($R = 0.53$–0.60) and mixed-layer CAPE ($R = 0.62$–0.70) show moderate-to-strong correlations. These values are significantly different from 0, at the 5% level, between WoFS and the radiosondes among all forecast lead times. However, both types of CAPE are overestimated, particularly for mixed-layer CAPE, at small observed magnitudes, as supported by large median absolute errors and linear regression fit intercepts. As an example, WoFS median mixed-layer CAPE among all forecast hour bins range from 27 to 98 J kg^{-1} compared to observed median values of 5–15 J kg^{-1}, when considering only those soundings with ≤300 J kg^{-1}. The overestimation of CAPE at these lower observed magnitudes may be due to the aforementioned stronger lapse rates and moister troposphere in WoFS.

CAPE in WoFS is also underestimated at the upper end of the observed distribution estimates, similar to prior non-TC studies using WoFS (Laser et al., 2022; Potvin et al., 2020). When considering observed soundings with

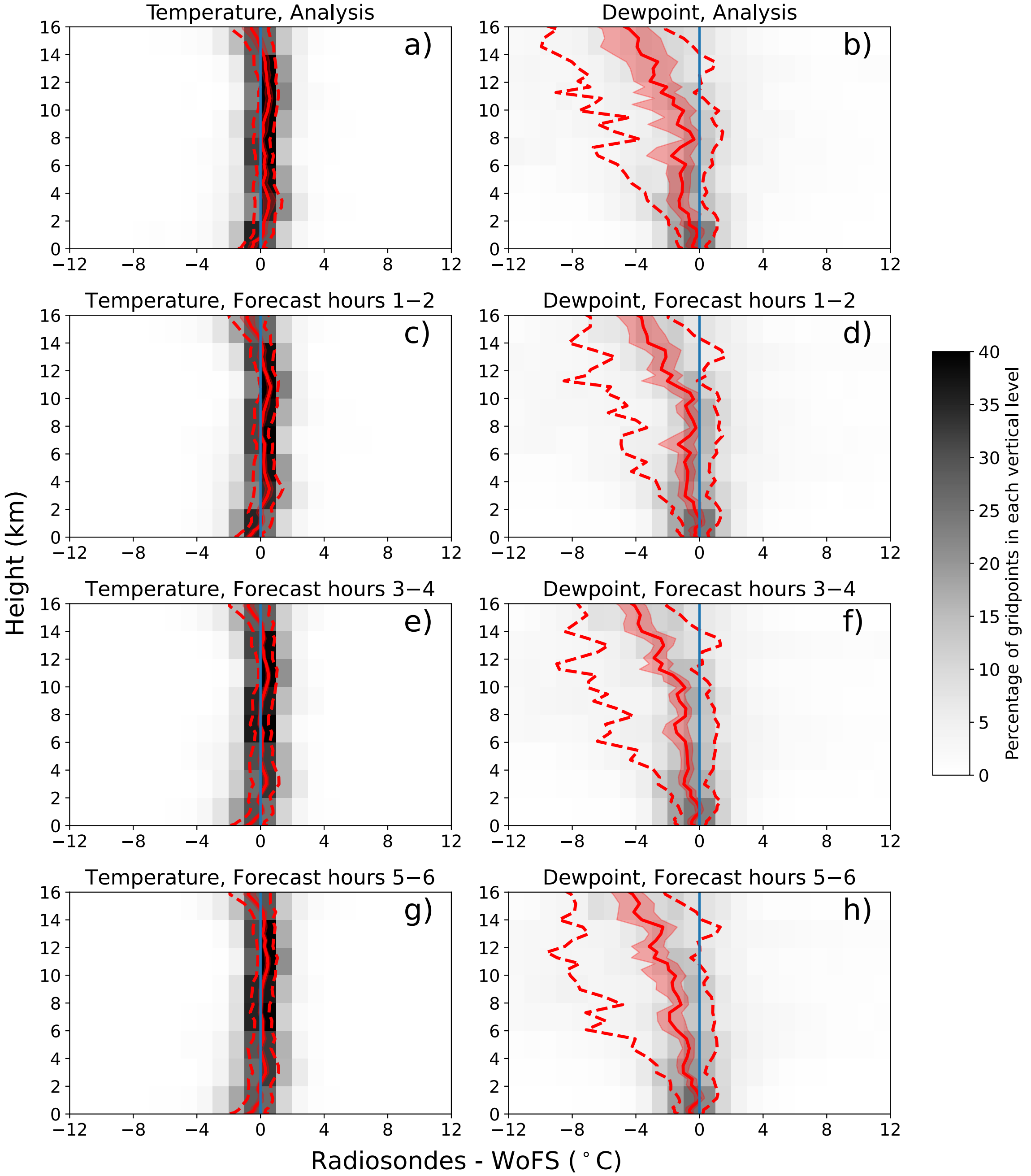

Figure 11. As in Figure 7, but for temperature (°C) and dewpoint (°C).

mixed-layer CAPE ≥1,200 J kg^{-1}, median WoFS values among forecast bins vary between 1,310– 1,613 J kg^{-1} compared to 1,784–1,972 J kg^{-1} in observations. Compared to those radiosondes exceeding the 100 J kg^{-1} threshold over the 0–3-km layer associated with TC tornadoes, only 46% of WoFS soundings also exceed this value (Baker et al., 2009; Eastin & Link, 2009). These significant differences in CAPE between WoFS and the radiosondes may be partially due to the magnifying properties of multivariate indices like CAPE, which can yield larger disparities than the base variables themselves. Neither the correlations nor the underestimation of CAPE varies significantly, at the 5% level, as a function of forecast lead time, despite the previously shown temperature biases that become stronger after the analysis.

Similar to the prior section, these results suggest that temperature and, to a lesser extent, dewpoint are reasonably represented in WoFS at all lead times, despite the occurrence of biases toward steeper lapse rates. However, both

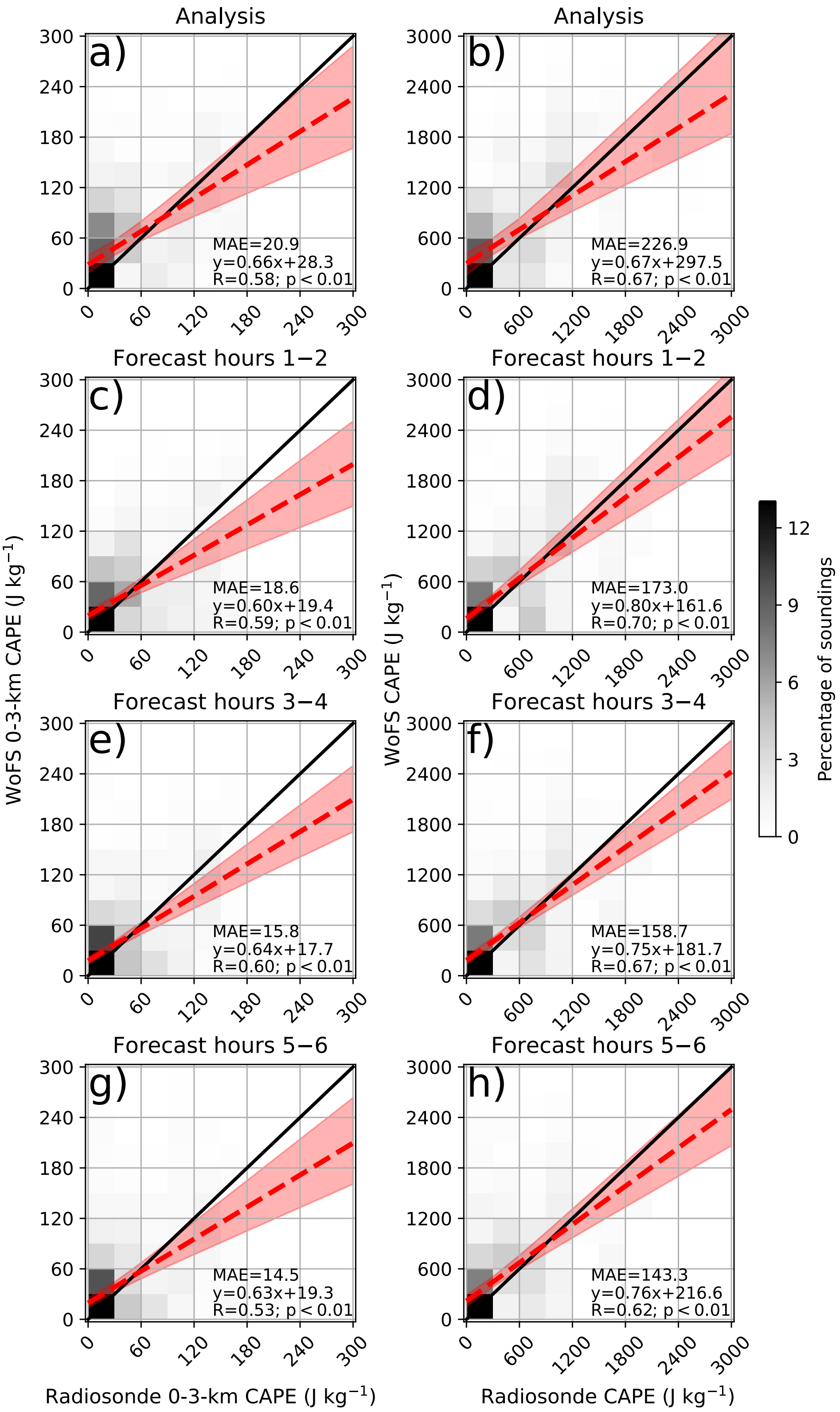

Figure 12. As in Figure 8, but for 0–3-km CAPE (J kg^{-1}) and mixed-layer CAPE (J kg^{-1}).

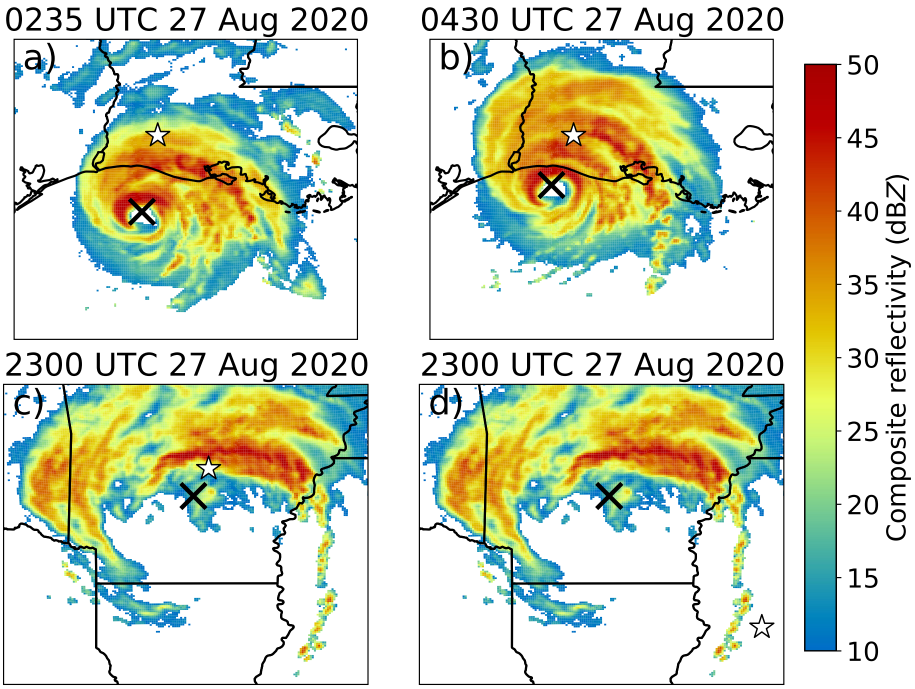

Figure 13. Plan view plot of four radiosonde launch locations (white stars), IBTrACS tropical cyclone center location (black Xs), and composite reflectivity (dBZ; shading) in Hurricane Laura (2020) from the Multi-Radar/Multi-Sensor product (Smith et al., 2016) for (a) 0235 UTC 27 August 2020 with observed maximum 10-m wind speed of 130 kt (National Severe Storms Laboratory (NSSL) radiosonde), (b) 0430 UTC 27 August 2020 with observed maximum 10-m wind speed of 130 kt (NSSL radiosonde), (c) 2300 UTC 27 August 2020 with observed maximum 10-m wind speed of 38 kt (National Weather Service (NWS) radiosonde), and (d) 2300 UTC 27 August 2020 with observed maximum 10-m wind speed of 38 kt (NWS radiosonde).

CAPE parameters studied are overestimated at lower observed values and underestimated at higher observed values. Challenges exist in the representation of convective-scale thermodynamic environments, especially above the surface in cloudy regions where observations are sparse and satellite radiances are unable to be assimilated (Derber & Wu, 1998; T. A. Jones et al., 2018). Some of this disagreement may also stem from the non-trivial uncertainty that exists in forecasting TC convective structure even within the analyses (Yussouf et al., 2020; Y. Wang et al., 2022). Accurate representation of TC outer rainbands in particular is key to properly simulating processes, including insolation-induced surface heating associated with any dry slots and cold pools associated with rainbands (Baker et al., 2009; Eastin et al., 2012). Sensitivity may also exist in the location of any potential midtropospheric dry air intrusions, which are hypothesized to contribute to tornado outbreaks (Baker et al., 2009; Curtis, 2004).

3.3. Case Study: Hurricane Laura (2020)

Hurricane Laura (2020) was chosen as our case study. Laura was the only case during our study period in which NSSL radiosondes were launched during WoFS forecasts, providing extra data at non-synoptic times. Hurricane Laura made landfall in western Louisiana as a category four hurricane with maximum 10-m winds of 130 kt and a minimum mean sea-level pressure of 931 hPa (Pasch et al., 2020). The strong intensity of Laura at landfall, together with the atypically large number of false alarm tornado warnings during 0235–2300 UTC 27 August 2020 (i.e., the study period), make this a notable case (i.e., 36 warnings and 2 tornado reports; IEM, 2020; Martinaitis, 2017). We have selected four radiosondes (i.e., two NWS and two NSSL radiosondes) to examine in the eastern half of the TC, where tornadoes typically occur (Hill et al., 1966; Novlan & Gray, 1974). The radiosondes were launched from 0235 UTC 27 August 2020 to 2300 UTC 27 August 2020. Note that one NSSL radiosonde (launched at 0235 UTC 27 August 2020) shown here only has limited data up through a ≈6-km height above the surface. This precludes the calculation of SRH in these cases due to insufficient data to calculate Bunkers storm motion vectors (Bunkers et al., 2014). The location of each radiosonde overlaid on the nearest

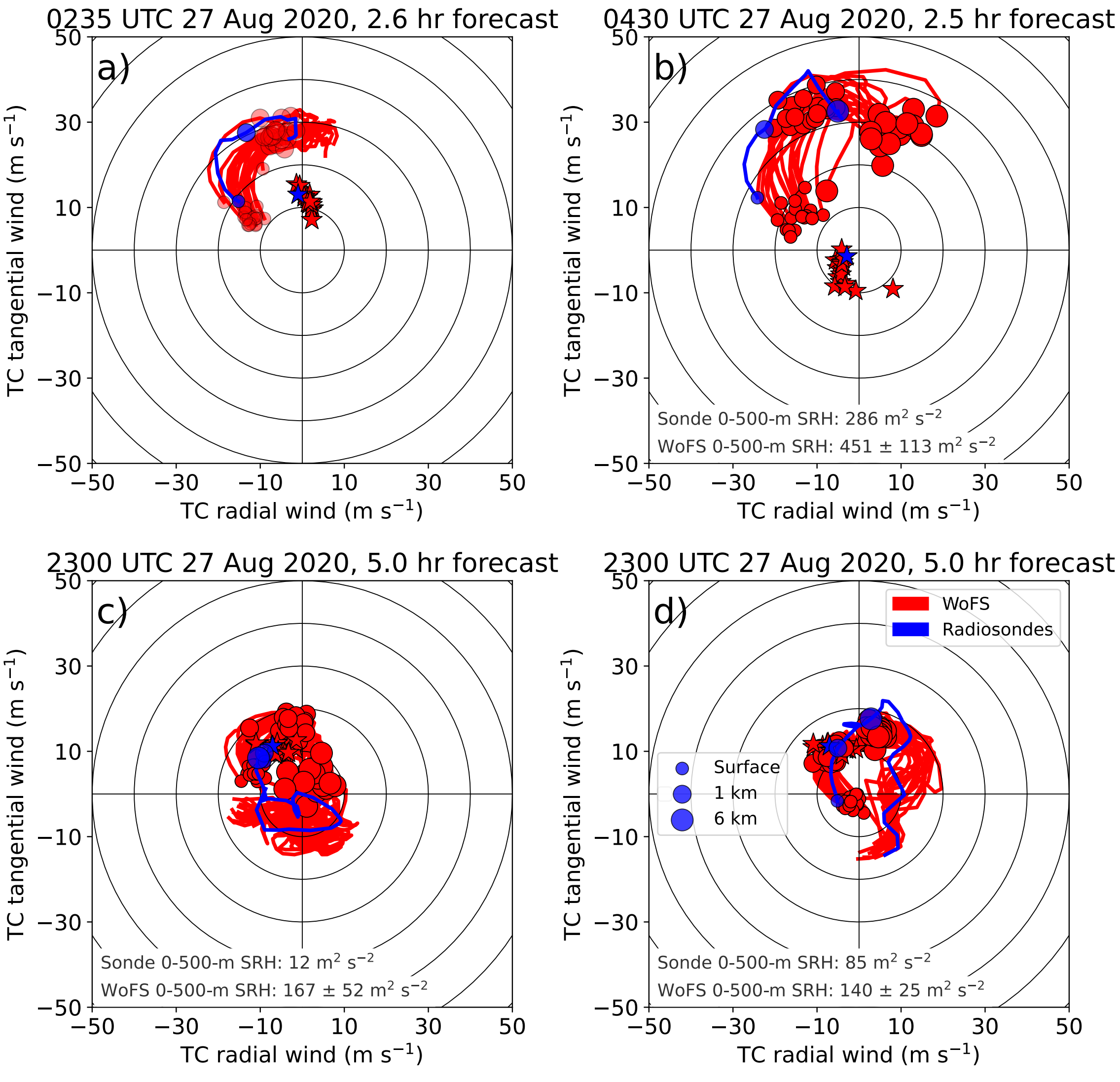

Figure 14. Hodograph of the tropical cyclone-relative radial wind (m s^{-1}) versus tangential wind (m s^{-1}) computed from radiosondes and the 18-member WoFS ensemble for Hurricane Laura (2020) at (a) 0235 UTC 27 August 2020, (b) 0430 UTC 27 August 2020, (c) 2300 UTC 27 August 2020, and (d) 2300 UTC 27 August 2020. The star shows the cell motion computed following (Bunkers et al., 2014). Winds at the surface, 1 km, and 6 km are shown using dots. Range rings are shown at 10 m s^{-1} intervals. Each hodograph has been smoothed in the vertical dimension with a 1–2–1 smoother. The 0–500-m storm-relative helicity (SRH) for the radiosondes along with the median and standard deviation of SRH among the WoFS ensemble members are shown. Panel (a) does not have SRH calculated due to the insufficient radiosonde data in the vertical to calculate the modified Bunkers cell-motion algorithm.

Multi-Radar/Multi-Sensor System reflectivity data (Smith et al., 2016) are shown in Figure 13. These four radiosondes are launched in a variety of locations, including both inner and outer TC rainbands, both near landfall with the TC near peak intensity, and well inland when the TC was a weak tropical storm. Comparison is made against forecasts at both shorter (i.e., 2.5–2.6 hr) and longer lead times (i.e., 5.0 hr).

The vertical structure of TC-relative winds in Hurricane Laura (2020) is shown using hodographs for each radiosonde and the associated WoFS-derived soundings in Figure 14. Except for Figure 14c, WoFS typically matches the shape of the observed hodograph, albeit smoother, as suggested by strong correlations of radial (R = 0.87–0.94) and tangential winds (R = 0.88–0.95) between the radiosondes and WoFS. However, WoFS underestimates the strength of the tangential and radial winds in the two radiosondes sampling the TC outer rainbands before landfall (Figures 14a and 14b), particularly in the lowest 3 km, such that the radiosonde hodographs mostly fall outside the ensemble envelope. Despite this underestimate, the lower-tropospheric vertical wind shear is stronger than observed in WoFS as supported by 0–500-m helicity for the radiosonde of 286 m^2 s^{-2} compared to median values for WoFS of 451 m^2 s^{-2}. The magnitude of TC winds is in better

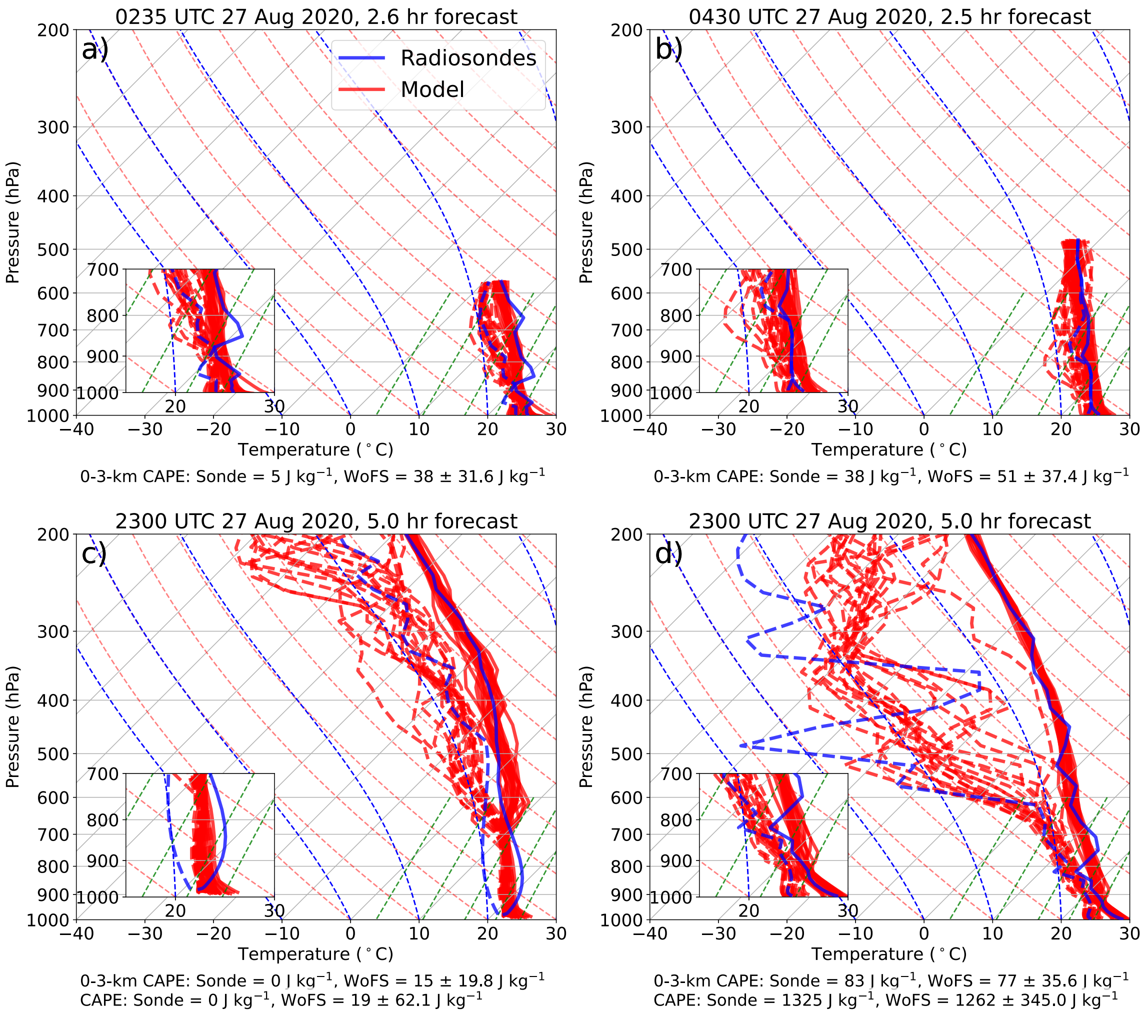

Figure 15. Skew T–*logp* diagram showing the temperature (°C; solid lines) and dewpoint (°C; dashed lines) from radiosondes and the 18-member WoFS ensemble for Hurricane Laura (2020) at (a) 0235 UTC 27 August 2020, (b) 0430 UTC 27 August 2020, (c) 2300 UTC 27 August 2020, and (d) 2300 UTC 27 August 2020. The 0–3-km CAPE and mixed-layer CAPE for the radiosondes, along with the median and standard deviation of 0–3-km CAPE and mixed-layer CAPE among the WoFS ensemble members are shown below each panel.

agreement following landfall near the eastern flank of the rainbands (Figure 14d). WoFS may have too much lower-tropospheric vertical wind shear in post-landfall soundings, as suggested by the stronger than observed 0–500-m SRH values (ensemble median of 140 m^2 s^{-2}) compared to the radiosondes (85 m^2 s^{-2}). Figure 14c shows that the strongest disagreement between WoFS and the radiosondes occurs directly to the south of the primary rainband in Hurricane Laura post-landfall (Figure 13c). Observed hodographs show very weak vertical wind shear below 6 km with small 0–500-m SRH (12 m^2 s^{-2}). In contrast, WoFS hodographs show TC winds that resemble the profiles in the remaining three panels associated with much stronger 0–500-m SRH (167 m^2 s^{-2}). Correlations between WoFS and the radiosondes are much lower for this radiosonde, especially for the radial winds ($R = 0.53$). This result is also consistent with its previously shown larger uncertainties compared to tangential winds. These differences may be partially associated with the location of this sounding in between the TC center and the primary rainband, such that small discrepancies in the TC center location can yield large differences in the winds (Nguyen et al., 2014; Ryglicki & Hart, 2015).

The vertical structure of temperature and, to a lesser extent, moisture from WoFS is also reasonably represented, although with smaller vertical variability in structure, compared to the radiosondes (Figure 15). Similar to the Skew *T*-log*p* composites, both WoFS data and the radiosonde located south of the primary TC rainband at landfall in Figure 12b, show a nearly saturated troposphere with approximately moist adiabatic lapse rates and small 0–3-

km CAPE values in WoFS (median of 38 J kg^{-1}) and the radiosonde (51 J kg^{-1}). Additionally, median absolute errors are low for temperature (1.0°C) and dewpoint (0.9°C). Additionally, correlation coefficients are also very strong for both variables between WoFS and the radiosondes ($R = 0.99$–1.00). However, WoFS does not simulate the remaining soundings as well (Figures 15a, 15c, and 15d). These radiosondes contain more substantial variability in temperature and dewpoint associated with temperature inversions and mid-to-upper-tropospheric dry layers, previously shown in landfalling TCs (Baker et al., 2009; Curtis, 2004). The dry layers are particularly pronounced in the post-landfall radiosondes, and the uncertainty of their representation in WoFS is comparable to that shown in WoFS forecasts of non-TC severe weather environments (Laser et al., 2022). Despite these disparities, modest agreement exists between WoFS and the radiosondes in Figures 14a, 14c, and 14d, which show: (a) 0–3-km CAPE from WoFS (median ranging from 15 to 77 J kg^{-1}) versus the radiosondes (0–83 J kg^{-1}) and (b) correlation coefficients for temperature ($R = 0.99$–1.00) and dewpoint ($R = 0.97$–0.99).

Together, these results suggest that the vertical structure of winds, temperature, and dewpoint are simulated with reasonable fidelity in Hurricane Laura (2020). More broadly, this case study shows general agreement with the results of the full sample shown in Sections 3.1 and 3.2. Nonetheless, these selected soundings suggest that WoFS occasionally underestimated the magnitude of TC winds and associated SRH, while showing deficiencies in the representation of temperature inversions and midtropospheric dry layers. This uncertainty is to be expected, due to potential errors in TC location and rainband structure at forecast lead times of up to 5 hr. This is especially true, given the strong horizontal gradients in winds, temperature, and moisture that can exist in TC rainbands (Eastin et al., 2012; McCaul et al., 2004). Additional uncertainty may have been introduced by the destruction of the Lake Charles WSR-88D radar at approximately 0600 UTC 27 Aug 2020, reducing the radar data available for assimilation in the post-landfall set of forecasts (i.e., Figures 13c and 13d; Pasch et al., 2020). Other sources of uncertainty are associated with the presence and structure of dry midtropospheric layers. These results suggest some caution should be exercised in using WoFS to identify favorable convective-scale thermodynamic environments, resulting from the non-trivial shortcomings associated with forecasting these dry layers.

4. Summary and Discussion

This study investigated the fidelity of severe convective weather environments in landfalling TCs as simulated by the Warn-on-Forecast System (WoFS). This analysis is a preliminary verification of WoFS performance in TCs due to the small sample size of landfalling TCs examined (i.e., 2020 hurricane season). Our study first examined the representation of convective-scale kinematic environments and their sensitivity to forecast lead time. The remainder of this work performed a similar assessment for convective-scale thermodynamic environments, followed by an analysis of the fidelity of WoFS simulated kinematic and thermodynamic environments at four sounding locations from Hurricane Laura (2020).

Convective-scale kinematic environments in WoFS were shown to reasonably match radiosonde data. WoFS and radiosondes showed strong near-surface vertical speed and directional shear, and veering and weakening of winds above this layer. Moderate-to-strong correlation coefficients together with comparable standard deviations for TC-relative radial and, especially, tangential winds between WoFS and the radiosondes suggest a fair representation of kinematic environments in WoFS. WoFS showed biases in TC winds, including: (a) weaker inflow throughout most of the troposphere and (b) stronger-than-observed near-surface tangential winds with weaker winds immediately above this layer. These biases became stronger after the analysis. WoFS also showed reasonable agreement with observed 0–500-m and 0–3-km SRH values, with greater error for stronger observed helicity values.

WoFS also reasonably forecasted convective-scale thermodynamic environments showing nearly moist adiabatic lapse rates associated with low CAPE. Specifically, the composite vertical structure of temperature and, to a lesser extent, dewpoint in WoFS was not significantly different from the radiosondes. Correlation coefficients were strong and standard deviations were comparable for either temperature and, less so, for dewpoint between WoFS and the radiosondes. Dewpoint above the boundary layer showed less agreement with near-surface values compared temperatures. WoFS showed a moist bias throughout the troposphere with steeper than observed lapse rates. These biases yielded a more unstable atmosphere, which may be one reason why WoFS overestimated CAPE and 0–3-km CAPE at low observed values. Similar to SRH, CAPE was underestimated at more extreme observed values in WoFS.

Analysis of soundings from Hurricane Laura (2020) showed general agreement with the composite sounding results. Specifically, TC-relative tangential and radial winds were reasonably represented, with a bias toward weaker-than-observed winds before TC landfall. Temperature and dewpoint in WoFS also agreed well with observations, but WoFS showed disparities in forecasting temperature inversions and mid- and upper-tropospheric dry layers.

In summary, these results show that WoFS simulates convective-scale kinematic and thermodynamic environments in landfalling TCs with reasonable fidelity. Forecasters should consider the convective-scale biases in WoFS shown above. Particular interest should be provided to the weaker than observed lower-tropospheric winds, and uncertainties associated with the location and magnitude of temperature inversions and dry layers, given their importance to TC tornadoes. These results also address the aforementioned questions raised in the Introduction:

- Is WoFS able to reasonably forecast convective-scale kinematic and thermodynamic environments in TCs?
  Yes, WoFS can forecast convective-scale kinematic and thermodynamic environments with reasonable fidelity. However, WoFS tends to underestimate TC winds and its associated vertical wind shear, while also showing biases toward more thermodynamically unstable environments for observed soundings with low CAPE.
- Does the fidelity of kinematic and thermodynamic convective-scale environments substantially degrade with increasing forecast lead time?
  WoFS shows small, non-significan increases in biases within convective-scale kinematic and thermodynamic environments with increasing forecast lead time.

Despite these uncertainties, WoFS provides the promise of eventually improving short-term TC tornado forecasts, which are strongly reliant on radar data and, tend to be lower skill than their non-TC counterparts (Martinaitis, 2017; Nowotarski et al., 2021). This analysis motivates a similar analysis of TC tornado proximity soundings, once a sufficiently large sample size exists, coincident with the period of WoFS availability. Prior work has shown that CAPE and SRH may be locally much higher in the near-supercell environment in TCs (Edwards, 2012; McCaul et al., 2004). A similar large-sample analysis of tornadic lower-tropospheric mesocyclone proxies in WoFS compared to observed radar data should also be undertaken, although recent case studies suggest that these forecasts may be less skillful, especially with increasing forecast lead time (T. A. Jones et al., 2019; Y. Wang et al., 2022). Verifying the forecasts of the structure and location of TC outer rainbands would also be useful, since most tornadoes occur there (Carroll-Smith et al., 2023; Edwards, 2012). Nonetheless, our incomplete physical understanding of the response of the TC rainbands to landfall may make the associated forecasts prone to particular uncertainty (Alford et al., 2020; May, 1996). Indeed, prior work has shown that these rainbands are associated with enhanced vertical wind shear, buoyancy, and potentially cold pools, suggesting that reasonable forecast location and structure of rainbands may help isolate mesoscale regions for forecasters to focus on (Eastin et al., 2012; McCaul et al., 2004). This may be a more modest goal than simulating low-topped supercells in TCs, which likely requires a much finer horizontal grid spacing than 3 km used in the current WoFS configuration (i.e., ≤1 km; Carroll-Smith et al., 2019; Morin & Parker, 2011). More broadly, this analysis raises questions about whether similar results also occur in convection-allowing operational models used for severe convective weather (High-Resolution Rapid Refresh; Dowell et al., 2022) versus those models used for TCs (i.e., Hurricane Analysis and Forecasting System, Hurricane Weather Research and Forecasting model; Gopalakrishnan et al., 2011; Hazelton et al., 2021).

Acknowledgments

This work is generously supported by funding from VORTEX-SE, NSF Grant AGS 2028151, NOAA/NIST Grant 70NANB19H056, NSSL Director's Discretionary Funds, and the NOAA/Office of Oceanic and Atmospheric Research under the NOAA-University of Oklahoma Cooperative Agreement NA21OAR4320204, U.S. Department of Commerce. The statements, findings, conclusions, and recommendations herein are those of the authors and do not necessarily reflect the views of NOAA, NSF, or NIST. We would like to thank Roger Edwards (SPC), two anonymous reviewers, Robert Rogers (HRD), Patrick Skinner (CIWRO/NSSL), Brian Matilla (CIWRO/NSSL), Holger Vömel (NCAR), Sim Aberson (HRD), Kathryn Sellwood (HRD), and Jonathan Zawislak (HRD) for critical and constructive feedback. This work would not have been possible without the IGRA radiosonde data from NOAA and IBTrACS data from NOAA/NCDC.

Data Availability Statement

TC track data were provided by NCEI (Knapp et al., 2010). NWS radiosonde data were provided by NOAA NCEI (Durre et al., 2006). NSSL radiosonde data were provided by Sean Waugh (Waugh, 2024). WoFS forecasts were provided by NSSL (Schenkel et al., 2024). All soundings and severe convective weather metrics were calculated using SHARPpy, version 1.4.0 (Blumberg et al., 2017), available under the SHARPpy license at https://sharp.weather.ou.edu/dev/index.html. All figures were made using Matplotlib, version 3.6.3 (Caswell et al., 2023; Hunter, 2007), available under the Matplotlib license at https://matplotlib.org/.

References

Alford, A. A., Zhang, J. A., Biggerstaff, M. I., Dodge, P., Marks, F. D., & Bodine, D. J. (2020). Transition of the hurricane boundary layer during the landfall of Hurricane Irene (2011). *Journal of the Atmospheric Sciences*, *77*(10), 3509–3531. https://doi.org/10.1175/jas-d-19-0290.1

Baker, A. K., Parker, M. D., & Eastin, M. D. (2009). Environmental ingredients for supercells and tornadoes within Hurricane Ivan. *Weather and Forecasting*, *24*(1), 223–244. https://doi.org/10.1175/2008waf2222146.1

Barnes, G., Zipser, E., Jorgensen, D., & Marks, F. (1983). Mesoscale and convective structure of a hurricane rainband. *Journal of the Atmospheric Sciences*, *40*(9), 2125–2137. https://doi.org/10.1175/1520-0469(1983)040<2125:macsoa>2.0.co;2

Benjamin, S. G., Weygandt, S. S., Brown, J. M., Hu, M., Alexander, C. R., Smirnova, T. G., et al. (2016). A North American hourly assimilation and model forecast cycle: The rapid refresh. *Monthly Weather Review*, *144*(4), 1669–1694. https://doi.org/10.1175/mwr-d-15-0242.1

Blumberg, W. G., Halbert, K. T., Supinie, T. A., Marsh, P. T., Thompson, R. L., & Hart, J. A. (2017). SHARPpy: An open-source sounding analysis toolkit for the atmospheric sciences. *Bulletin America Meteorology Social*, *98*(8), 1625–1636. https://doi.org/10.1175/bams-d-15-00309.1

Bogner, P. B., Barnes, G. M., & Franklin, J. L. (2000). Conditional instability and shear for six hurricanes over the Atlantic Ocean. *Weather and Forecasting*, *15*(2), 192–207. https://doi.org/10.1175/1520-0434(2000)015<0192:ciasfs>2.0.co;2

Bray, M. T., Turner, D. D., & de Boer, G. (2021). Evaluation of the rapid refresh numerical weather prediction model over Arctic Alaska. *Weather and Forecasting*, *36*(3), 1061–1077. https://doi.org/10.1175/waf-d-20-0169.1

Bunkers, M. J., Barber, D. A., Thompson, R. L., Edwards, R., & Garner, J. (2014). Choosing a universal mean wind for supercell motion prediction. *Journal of Operational Meteorology*, *2*(11), 115–129. https://doi.org/10.15191/nwajom.2014.0211

Bunkers, M. J., Klimowski, B. A., Zeitler, J. W., Thompson, R. L., & Weisman, M. L. (2000). Predicting supercell motion using a new hodograph technique. *Weather and Forecasting*, *15*(1), 61–79. https://doi.org/10.1175/1520-0434(2000)015<0061:psmuan>2.0.co;2

Carroll-Smith, D. L., Dawson, L. C., & Trapp, R. J. (2019). High resolution real-data WRF modeling and verification of tropical cyclone tornadoes associated with Hurricane Ivan 2004. *E-Journal of Severe Storms Meteorology*, *14*(2), 1–36. https://doi.org/10.55599/ejssm.v14i2.72

Carroll-Smith, D. L., Green, B. W., Edwards, R., Bai, L., Litta, A., Huang, X., et al. (2023). Forecasting tropical cyclone tornadoes and impacts: Report from IWTC-X. *Tropical Cyclone Research and Review*, *12*(2), 123–135. https://doi.org/10.1016/j.tcrr.2023.06.003

Caswell, T. A., Lee, A., Droettboom, M., de Andrade, E. S., Hoffman, T., Klymak, J., et al. (2023). matplotlib/matplotlib: Rel: v3.6.3 [software]. https://doi.org/10.5281/zenodo.7527665

Chavas, D. R., & Emanuel, K. (2010). A QuikSCAT climatology of tropical cyclone size. *Geophysical Research Letters*, *37*(18), L18816. https://doi.org/10.1029/2010gl044558

Chrisman, J. (2011). Supplemental adaptive intra-volume low-level scan (SAILS) (Tech. Rep.). Retrieved from http://www.roc.noaa.gov/wsr88d/PublicDocs/NewTechnology/SAILS_Initial_Presentation_Sep_2011.pdf

Clark, A. J., & Loken, E. D. (2022). Machine learning–derived severe weather probabilities from a Warn-on-Forecast system. *Weather and Forecasting*, *37*(10), 1721–1740. https://doi.org/10.1175/waf-d-22-0056.1

Coffer, B. E., Parker, M. D., Thompson, R. L., Smith, B. T., & Jewell, R. E. (2019). Using near-ground storm relative helicity in supercell tornado forecasting. *Weather and Forecasting*, *34*(5), 1417–1435. https://doi.org/10.1175/waf-d-19-0115.1

Coniglio, M. C. (2012). Verification of RUC 0–1-h forecasts and SPC mesoscale analyses using VORTEX2 soundings. *Weather and Forecasting*, *27*(3), 667–683. https://doi.org/10.1175/waf-d-11-00096.1

Coniglio, M. C., Correia, J., Marsh, P. T., & Kong, F. (2013). Verification of convection-allowing WRF model forecasts of the planetary boundary layer using sounding observations. *Weather and Forecasting*, *28*(3), 842–862. https://doi.org/10.1175/waf-d-12-00103.1

Coniglio, M. C., & Parker, M. D. (2020). Insights into supercells and their environments from three decades of targeted radiosonde observations. *Monthly Weather Review*, *148*(12), 4893–4915. https://doi.org/10.1175/mwr-d-20-0105.1

Curtis, L. (2004). Midlevel dry intrusions as a factor in tornado outbreaks associated with landfalling tropical cyclones from the Atlantic and Gulf of Mexico. *Weather and Forecasting*, *19*(2), 411–427. https://doi.org/10.1175/1520-0434(2004)019<0411:mdiaaf>2.0.co;2

Davies-Jones, R. (1984). Streamwise vorticity: The origin of updraft rotation in supercell storms. *Journal of the Atmospheric Sciences*, *41*(20), 2991–3006. https://doi.org/10.1175/1520-0469(1984)041<2991:svtoou>2.0.co;2

Davis, C., Brown, B., & Bullock, R. (2006). Object-based verification of precipitation forecasts. Part I: Methodology and application to mesoscale rain areas. *Monthly Weather Review*, *134*(7), 1772–1784. https://doi.org/10.1175/mwr3145.1

Dawson, D. T., Wicker, L. J., Mansell, E. R., & Tanamachi, R. L. (2012). Impact of the environmental low-level wind profile on ensemble forecasts of the 4 May 2007 Greensburg, Kansas, tornadic storm and associated mesocyclones. *Monthly Weather Review*, *140*(2), 696–716. https://doi.org/10.1175/mwr-d-11-00008.1

Derber, J., & Wu, W. (1998). The use of TOVS cloud-cleared radiances in the NCEP SSI analysis system. *Monthly Weather Review*, *126*(8), 2287–2299. https://doi.org/10.1175/1520-0493(1998)126<2287:tuotcc>2.0.co;2

Devanas, A., Gregoria, D., Kasper, K., & Santos, P. (2008). Tropical cyclone induced tornadoes associated with the formation of Tropical Storm Barry. In *20th Conference on Climate Variability and Change* (p. JP.3). New Orleans.

Developmental Testbed Center. (2008). A description of the advanced research WRF version 3 NCAR Tech. Note NCAR/TN-475+STR (p. 113).

Didlake, A. C., & Houze, R. A. (2009). Convective-scale downdrafts in the principal rainband of Hurricane Katrina (2005). *Monthly Weather Review*, *137*(10), 3269–3293. https://doi.org/10.1175/2009mwr2827.1

Ditchek, S. D., Corbosiero, K. L., Fovell, R. G., & Molinari, J. (2020). Electrically active diurnal pulses in Hurricane Harvey (2017). *Monthly Weather Review*, *148*(6), 2283–2305. https://doi.org/10.1175/mwr-d-20-0022.1

Dowell, D. C., Alexander, C., Beck, J., Benjamin, S., Hu, M., Ladwig, T., et al. (2016). Development of a high-resolution rapid refresh ensemble (HRRRE) for severe weather forecasting. In *28th Conference on Severe Local Storms*.

Dowell, D. C., Alexander, C. R., James, E. P., Weygandt, S. S., Benjamin, S. G., Manikin, G. S., et al. (2022). The High-Resolution Rapid Refresh (HRRR): An hourly updating convection-allowing forecast model. Part I: Motivation and system description. *Weather and Forecasting*, *37*(8), 1371–1395. https://doi.org/10.1175/waf-d-21-0151.1

Dudhia, J. (1989). Numerical study of convection observed during the winter monsoon experiment using a mesoscale two-dimensional model. *Journal of the Atmospheric Sciences*, *46*(20), 3077–3107. https://doi.org/10.1175/1520-0469(1989)046<3077:nsocod>2.0.co;2

Duran, P., & Molinari, J. (2016). Upper-tropospheric low Richardson number in tropical cyclones: Sensitivity to cyclone intensity and the diurnal cycle. *Journal of the Atmospheric Sciences*, *73*(2), 545–554. https://doi.org/10.1175/jas-d-15-0118.1

Durre, I., Vose, R. S., & Wuertz, D. B. (2006). Overview of the integrated global radiosonde archive [Dataset]. *Journal of Climate*, *19*(1), 53–68. https://doi.org/10.1175/jcli3594.1

Eastin, M. D., Gardner, T. L., Link, M. C., & Smith, K. C. (2012). Surface cold pools in the outer rainbands of Tropical Storm Hanna (2008) near landfall. *Monthly Weather Review*, *140*(2), 471–491. https://doi.org/10.1175/mwr-d-11-00099.1

Eastin, M. D., & Link, M. C. (2009). Miniature supercells in an offshore outer rainband of Hurricane Ivan (2004). *Monthly Weather Review*, *137*(7), 2081–2104. https://doi.org/10.1175/2009mwr2753.1

Edwards, R. (2012). Tropical cyclone tornadoes: A review of knowledge in research and prediction. *The Electronic Journal of Severe Storms Meteorology*, *7*(6), 1–61. https://doi.org/10.55599/ejssm.v7i6.42

Edwards, R., Dean, A. R., Thompson, R. L., & Smith, B. T. (2012). Convective modes for significant severe thunderstorms in the contiguous United States. Part III: Tropical cyclone tornadoes. *Weather and Forecasting*, *27*(6), 1507–1519. https://doi.org/10.1175/waf-d-11-00117.1

Edwards, R., & Pietrycha, A. (2006). Archetypes for surface baroclinic boundaries influencing tropical cyclone tornado occurrence. In *23rd Conference on Severe Local Storms* (p. P8.2). St. Louis, MO.

Edwards, R., & Thompson, R. (2012). Reversible CAPE in tropical cyclone tornado regimes. In *Proceeding of 27th Conference on Severe Local Storms* (p. 88).

Evans, C., Wood, K. M., Aberson, S. D., Archambault, H. M., Milrad, S. M., Bosart, L. F., et al. (2017). The extratropical transition of tropical cyclones. Part I: Cyclone evolution and direct impacts. *Monthly Weather Review*, *145*(11), 4317–4344. https://doi.org/10.1175/mwr-d-17-0027.1

Fischer, M. S., Reasor, P. D., Rogers, R. F., & Gamache, J. F. (2022). An analysis of tropical cyclone vortex and convective characteristics in relation to storm intensity using a novel airborne Doppler radar database. *Monthly Weather Review*, *150*(9), 2255–2278. https://doi.org/10.1175/mwr-d-21-0223.1

Flora, M. L., Potvin, C. K., Skinner, P. S., Handler, S., & McGovern, A. (2021). Using machine learning to generate storm-scale probabilistic guidance of severe weather hazards in the Warn-on-Forecast system. *Monthly Weather Review*, *149*(5), 1535–1557. https://doi.org/10.1175/mwr-d-20-0194.1

Frank, W. (1977). The structure and energetics of the tropical cyclone. Part I: Storm structure. *Monthly Weather Review*, *105*(9), 1119–1135. https://doi.org/10.1175/1520-0493(1977)105<1119:tsaeot>2.0.co;2

Franklin, J., Black, M., & Valde, K. (2003). GPS dropwindsonde wind profiles in hurricanes and their operational implications. *Weather and Forecasting*, *18*(1), 32–44. https://doi.org/10.1175/1520-0434(2003)018<0032:gdwpih>2.0.co;2

Gal-Chen, T., & Somerville, R. C. (1975). On the use of a coordinate transformation for the solution of the Navier-Stokes equations. *Journal of Computational Physics*, *17*(2), 209–228. https://doi.org/10.1016/0021-9991(75)90037-6

Gentry, R. C. (1983). Genesis of tornadoes associated with hurricanes. *Monthly Weather Review*, *111*(9), 1793–1805. https://doi.org/10.1175/1520-0493(1983)111<1793:gotawh>2.0.co;2

Gopalakrishnan, S. G., Marks, F., Zhang, X., Bao, J.-W., Yeh, K.-S., & Atlas, R. (2011). The experimental HWRF system: A study on the influence of horizontal resolution on the structure and intensity changes in tropical cyclones using an idealized framework. *Monthly Weather Review*, *139*(6), 1762–1784. https://doi.org/10.1175/2010mwr3535.1

Green, B. W., Zhang, F., & Markowski, P. (2011). Multiscale processes leading to supercells in the landfalling outer rainbands of Hurricane Katrina (2005). *Weather and Forecasting*, *26*(6), 828–847. https://doi.org/10.1175/waf-d-10-05049.1

Hazelton, A., Zhang, Z., Liu, B., Dong, J., Alaka, G., Wang, W., et al. (2021). 2019 Atlantic hurricane forecasts from the global-nested Hurricane Analysis and Forecast System: Composite statistics and key events. *Weather and Forecasting*, *36*(2), 519–538. https://doi.org/10.1175/waf-d-20-0044.1

Hence, D. A., & Houze, R. A. (2008). Kinematic structure of convective-scale elements in the rainbands of Hurricanes Katrina and Rita (2005). *Journal of Geophysical Research*, *113*(D15), D15108. https://doi.org/10.1029/2007jd009429

Hendricks, E. A., Knievel, J. C., & Nolan, D. S. (2021). Evaluation of boundary layer and urban canopy parameterizations for simulating wind in Miami during Hurricane Irma (2017). *Monthly Weather Review*, *149*, 2321–2349. https://doi.org/10.1175/mwr-d-20-0278.1

Hill, E., Malkin, W., & Schulz, W. (1966). Tornadoes associated with cyclones of tropical origin—Practical features. *Journal of Applied Meteorology and Climatology*, *5*(6), 745–763. https://doi.org/10.1175/1520-0450(1966)005<0745:tawcot>2.0.co;2

Hlywiak, J., & Nolan, D. S. (2022). The evolution of asymmetries in the tropical cyclone boundary layer wind field during landfall. *Monthly Weather Review*, *150*(3), 529–549. https://doi.org/10.1175/mwr-d-21-0191.1

Hong, S.-Y., Noh, Y., & Dudhia, J. (2006). A new vertical diffusion package with an explicit treatment of entrainment processes. *Monthly Weather Review*, *134*(9), 2318–2341. https://doi.org/10.1175/mwr3199.1

Houtekamer, P. L., Mitchell, H. L., Pellerin, G., Buehner, M., Charron, M., Spacek, L., & Hansen, B. (2005). Atmospheric data assimilation with an ensemble Kalman filter: Results with real observations. *Monthly Weather Review*, *133*(3), 604–620. https://doi.org/10.1175/mwr-2864.1

Hunter, J. D. (2007). Matplotlib: A 2D graphics environment [Software]. *Computer Science and Engineering*, *9*(3), 90–95. https://doi.org/10.1109/mcse.2007.55

Iacono, M. J., Delamere, J. S., Mlawer, E. J., Shephard, M. W., Clough, S. A., & Collins, W. D. (2008). Radiative forcing by long-lived greenhouse gases: Calculations with the AER radiative transfer models. *Journal of Geophysical Research*, *113*(D13). https://doi.org/10.1029/2008jd009944

IEM. (2020). Iowa Environmental Mesonet (IEM) radar and warning viewer (Tech. Rep.). Retrieved from http://mesonet.agron.iastate.edu/GIS/apps/rview/warnings.phtml

Janjić, Z. I. (1994). The step-mountain eta coordinate model: Further developments of the convection, viscous sublayer, and turbulence closure schemes. *Monthly Weather Review*, *122*(5), 927–945. https://doi.org/10.1175/1520-0493(1994)122<0927:tsmecm>2.0.co;2

Jones, S. C., Harr, P. A., Abraham, J., Bosart, L. F., Bowyer, P. J., Evans, J. L., et al. (2003). The extratropical transition of tropical cyclones: Forecast challenges, current understanding, and future directions. *Weather and Forecasting*, *18*(6), 1052–1092. https://doi.org/10.1175/1520-0434(2003)018<1052:tetotc>2.0.co;2

Jones, T. A., Knopfmeier, K., Wheatley, D., Creager, G., Minnis, P., & Palikonda, R. (2016). Storm-scale data assimilation and ensemble forecasting with the NSSL experimental Warn-on-Forecast system. Part II: Combined radar and satellite data experiments. *Weather and Forecasting*, *31*(1), 297–327. https://doi.org/10.1175/waf-d-15-0107.1

Jones, T. A., Skinner, P., Yussouf, N., Knopfmeier, K., Reinhart, A., & Dowell, D. (2019). Forecasting high-impact weather in landfalling tropical cyclones using a Warn-on-Forecast system. *Bulletin America Meteorology Social*, *100*(8), 1405–1417. https://doi.org/10.1175/bams-d-18-0203.1

Jones, T. A., Wang, X., Skinner, P., Johnson, A., & Wang, Y. (2018). Assimilation of GOES-13 imager clear-sky water vapor (6.5 μm) radiances into a Warn-on-Forecast system. *Monthly Weather Review*, *146*(4), 1077–1107. https://doi.org/10.1175/mwr-d-17-0280.1

Kleist, D. T., Parrish, D. F., Derber, J. C., Treadon, R., Wu, W.-S., & Lord, S. (2009). Introduction of the GSI into the NCEP global data assimilation system. *Weather and Forecasting*, *24*(6), 1691–1705. https://doi.org/10.1175/2009waf2222201.1

Knapp, K. R., Kruk, M. C., Levinson, D. H., Diamond, H. J., & Neumann, C. J. (2010). The international best track archive for climate stewardship (IBTrACS) unifying tropical cyclone data [Dataset]. *Bulletin America Meteorology Social*, *91*(3), 363–376. https://doi.org/10.1175/2009bams2755.1

Knupp, K. R., Walters, J., & Biggerstaff, M. (2006). Doppler profiler and radar observations of boundary layer variability during the landfall of Tropical Storm Gabrielle. *Journal of the Atmospheric Sciences*, *63*(1), 234–251. https://doi.org/10.1175/jas3608.1

Landsea, C. W., & Franklin, J. L. (2013). Atlantic hurricane database uncertainty and presentation of a new database format [Dataset]. *Monthly Weather Review*, *141*(10), 3576–3592. https://doi.org/10.1175/mwr-d-12-00254.1

Laser, J. J., Coniglio, M. C., Skinner, P. S., & Smith, E. N. (2022). Doppler lidar and mobile radiosonde observation-based evaluation of Warn-on-Forecast System predicted near-supercell environments during TORUS 2019. *Weather and Forecasting*, *37*(10), 1783–1804. https://doi.org/10.1175/waf-d-21-0190.1

Lawson, J. R., Kain, J. S., Yussouf, N., Dowell, D. C., Wheatley, D. M., Knopfmeier, K. H., & Jones, T. A. (2018). Advancing from convection-allowing NWP to warn-on-forecast: Evidence of progress. *Weather and Forecasting*, *33*(2), 599–607. https://doi.org/10.1175/waf-d-17-0145.1

MacDonald, L. M., & Nowotarski, C. J. (2023). Verification of rapid refresh and high-resolution rapid refresh model variables in tornadic tropical cyclones. *Weather and Forecasting*, *38*(5), 655–675. https://doi.org/10.1175/waf-d-22-0117.1

Mansell, E. R., Ziegler, C. L., & Bruning, E. C. (2010). Simulated electrification of a small thunderstorm with two-moment bulk microphysics. *Journal of the Atmospheric Sciences*, *67*(1), 171–194. https://doi.org/10.1175/2009jas2965.1

Martinaitis, S. M. (2017). Radar observations of tornado-warned convection associated with tropical cyclones over Florida. *Weather and Forecasting*, *32*(1), 165–186. https://doi.org/10.1175/waf-d-16-0105.1

May, P. T. (1996). The organization of convection in the rainbands of Tropical Cyclone Laurence. *Monthly Weather Review*, *124*(5), 807–815. https://doi.org/10.1175/1520-0493(1996)124<0807:toocit>2.0.co;2

McCaul, E. W. (1987). Observations of the hurricane "Danny" tornado outbreak of 16 August 1985. *Monthly Weather Review*, *115*(6), 1206–1223. https://doi.org/10.1175/1520-0493(1987)115<1206:oothto>2.0.co;2

McCaul, E. W. (1991). Buoyancy and shear characteristics of hurricane-tornado environments. *Monthly Weather Review*, *119*(8), 1954–1978. https://doi.org/10.1175/1520-0493(1991)119<1954:bascoh>2.0.co;2

McCaul, E. W., Buechler, D. E., Goodman, S. J., & Cammarata, M. (2004). Doppler radar and lightning network observations of a severe outbreak of tropical cyclone tornadoes. *Monthly Weather Review*, *132*(7), 1747–1763. https://doi.org/10.1175/1520-0493(2004)132<1747:dralno>2.0.co;2

McCaul, E. W., & Weisman, M. L. (1996). Simulations of shallow supercell storms in landfalling hurricane environments. *Monthly Weather Review*, *124*(3), 408–429. https://doi.org/10.1175/1520-0493(1996)124<0408:sosssi>2.0.co;2

Merrill, R. (1984). A comparison of large and small tropical cyclones. *Monthly Weather Review*, *112*(7), 1408–1418. https://doi.org/10.1175/1520-0493(1984)112<1408:acolas>2.0.co;2

Mlawer, E. J., Taubman, S. J., Brown, P. D., Iacono, M. J., & Clough, S. A. (1997). Radiative transfer for inhomogeneous atmospheres: RRTM, a validated correlated-k model for the longwave. *Journal of Geophysical Research*, *102*(D14), 16663–16682. https://doi.org/10.1029/97jd00237

Molinari, J., Romps, D. M., Vollaro, D., & Nguyen, L. (2012). CAPE in tropical cyclones. *Journal of the Atmospheric Sciences*, *69*(8), 2452–2463. https://doi.org/10.1175/jas-d-11-0254.1

Molinari, J., & Vollaro, D. (2008). Extreme helicity and intense convective towers in Hurricane Bonnie. *Monthly Weather Review*, *136*(11), 4355–4372. https://doi.org/10.1175/2008mwr2423.1

Molinari, J., & Vollaro, D. (2010). Distribution of helicity, CAPE, and shear in tropical cyclones. *Journal of the Atmospheric Sciences*, *67*(1), 274–284. https://doi.org/10.1175/2009jas3090.1

Morin, M. J., & Parker, M. D. (2011). A numerical investigation of supercells in landfalling tropical cyclones. *Geophysical Research Letters*, *38*(10), L10801. https://doi.org/10.1029/2011gl047448

Morotomi, K., Shimamura, S., Kobayashi, F., Takamura, T., Takano, T., Higuchi, A., & Iwashita, H. (2020). Evolution of a tornado and debris ball associated with Super Typhoon Hagibis 2019 observed by x-band phased array weather radar in Japan. *Geophysical Research Letters*, *47*(24), e2020GL091061. https://doi.org/10.1029/2020gl091061

Nakanishi, M., & Niino, H. (2004). An improved Mellor–Yamada level-3 model with condensation physics: Its design and verification. *Boundary-Layer Meteorology*, *112*, 1–31. https://doi.org/10.1023/b:boun.0000020164.04146.98

Nguyen, L. T., Molinari, J., & Thomas, D. (2014). Evaluation of tropical cyclone center identification methods in numerical models. *Monthly Weather Review*, *142*(11), 4326–4339. https://doi.org/10.1175/mwr-d-14-00044.1

Novlan, D. J., & Gray, W. M. (1974). Hurricane-spawned tornadoes. *Monthly Weather Review*, *102*(7), 476–488. https://doi.org/10.1175/1520-0493(1974)102<0476:hst>2.0.co;2

Nowotarski, C. J., Spotts, J., Edwards, R., Overpeck, S., & Woodall, G. R. (2021). Tornadoes in Hurricane Harvey. *Weather and Forecasting*, *36*(5), 1589–1609. https://doi.org/10.1175/waf-d-20-0196.1

Onderlinde, M. J., & Nolan, D. S. (2014). Environmental helicity and its effects on development and intensification of tropical cyclones. *Journal of the Atmospheric Sciences*, *71*(11), 4308–4320. https://doi.org/10.1175/jas-d-14-0085.1

Parker, M. D. (2014). Composite VORTEX2 supercell environments from near-storm soundings. *Monthly Weather Review*, *142*(2), 508–529. https://doi.org/10.1175/mwr-d-13-00167.1

Pasch, R., Berg, R., Roberts, D. R., & Papin, P. P. (2020). Tropical cyclone report: Hurricane Laura (20 August–29 August 2020) (Tech. Rep.). Retrieved from https://www.nhc.noaa.gov/data/tcr/AL132020_Laura.pdf

Potvin, C. K., & Flora, M. L. (2015). Sensitivity of idealized supercell simulations to horizontal grid spacing: Implications for Warn-on-Forecast. *Monthly Weather Review*, *143*(8), 2998–3024. https://doi.org/10.1175/mwr-d-14-00416.1

Potvin, C. K., Skinner, P. S., Hoogewind, K. A., Coniglio, M. C., Gibbs, J. A., Clark, A. J., et al. (2020). Assessing systematic impacts of PBL schemes on storm evolution in the NOAA Warn-on-Forecast System. *Monthly Weather Review*, *148*(6), 2567–2590. https://doi.org/10.1175/mwr-d-19-0389.1

Rappaport, E. N. (2014). Fatalities in the United States from Atlantic tropical cyclones: New data and interpretation. *Bulletin America Meteorology Social*, *95*(3), 341–346. https://doi.org/10.1175/bams-d-12-00074.1

Reasor, P. D., Rogers, R., & Lorsolo, S. (2013). Environmental flow impacts on tropical cyclone structure diagnosed from airborne Doppler radar composites. *Monthly Weather Review*, *141*(9), 2949–2969. https://doi.org/10.1175/mwr-d-12-00334.1

Rios-Berrios, R., Davis, C. A., & Torn, R. D. (2018). A hypothesis for the intensification of tropical cyclones under moderate vertical wind shear. *Journal of the Atmospheric Sciences*, *75*(12), 4149–4173. https://doi.org/10.1175/jas-d-18-0070.1

Rios-Berrios, R., & Torn, R. D. (2017). Climatological analysis of tropical cyclone intensity changes under moderate vertical wind shear. *Monthly Weather Review*, *145*(5), 1717–1738. https://doi.org/10.1175/mwr-d-16-0350.1

Rios-Berrios, R., Torn, R. D., & Davis, C. A. (2016). An ensemble approach to investigate tropical cyclone intensification in sheared environments. Part I: Katia (2011). *Journal of the Atmospheric Sciences*, *73*(1), 71–93. https://doi.org/10.1175/jas-d-15-0052.1

Ryglicki, D. R., & Hart, R. E. (2015). An investigation of center-finding techniques for tropical cyclones in mesoscale models. *Journal of Applied Meteorology and Climatology*, *54*(4), 825–846. https://doi.org/10.1175/jamc-d-14-0106.1

Schenkel, B. A., Calhoun, K., Sandmæl, T., Fruits, Z., Schick, I., Ake, M. C., & Kassel, B. F. (2023). Lightning and radar characteristics of tornadoes in landfalling tropical cyclones. *Journal of Geophysical Research: Atmospheres*, *128*(16), e2023JD038685. https://doi.org/10.1029/2023jd038685

Schenkel, B. A., Coniglio, M., & Edwards, R. (2021). How does the relationship between ambient deep-tropospheric vertical wind shear and tropical cyclone tornadoes change between coastal and inland environments? *Weather and Forecasting*, *36*(2), 539–566. https://doi.org/10.1175/waf-d-20-0127.1

Schenkel, B. A., Edwards, R., & Coniglio, M. (2020). A climatological analysis of ambient deep-tropospheric vertical wind shear impacts upon tornadic supercells in tropical cyclones. *Weather and Forecasting*, *35*(5), 2033–2059. https://doi.org/10.1175/waf-d-19-0220.1

Schenkel, B. A., Jones, T., & Waugh, S. (2024). Warn-on-Forecast, NWS, and NSSL soundings associated with “Assessing the fidelity of landfalling tropical cyclone convective-scale environments in the Warn-on-Forecast System using radiosondes” [Data]. https://zenodo.org/records/10689798

Schultz, C. J., Petersen, W. A., & Carey, L. D. (2009). Preliminary development and evaluation of lightning jump algorithms for the real-time detection of severe weather. *Journal of Applied Meteorology and Climatology*, *48*(12), 2543–2563. https://doi.org/10.1175/2009jamc2237.1

Schultz, L. A., & Cecil, D. J. (2009). Tropical cyclone tornadoes, 1950–2007. *Monthly Weather Review*, *137*(10), 3471–3484. https://doi.org/10.1175/2009mwr2896.1

Skinner, P. S., Wheatley, D. M., Knopfmeier, K. H., Reinhart, A. E., Choate, J. J., Jones, T. A., et al. (2018). Object-based verification of a prototype Warn-on-Forecast system. *Weather and Forecasting*, *33*(5), 1225–1250. https://doi.org/10.1175/waf-d-18-0020.1

Smith, T. M., Lakshmanan, V., Stumpf, G. J., Ortega, K. L., Hondl, K., Cooper, K., et al. (2016). Multi-Radar Multi-Sensor (MRMS) severe weather and aviation products: Initial operating capabilities [Dataset]. *Bulletin America Meteorology Social*, *97*(9), 1617–1630. https://doi.org/10.1175/bams-d-14-00173.1

Stern, D. P., Bryan, G. H., & Aberson, S. D. (2016). Extreme low-level updrafts and wind speeds measured by dropsondes in tropical cyclones. *Monthly Weather Review*, *144*(6), 2177–2204. https://doi.org/10.1175/mwr-d-15-0313.1

Stern, D. P., & Nolan, D. (2012). On the height of the warm core in tropical cyclones. *Journal of the Atmospheric Sciences*, *69*(5), 1657–1680. https://doi.org/10.1175/jas-d-11-010.1

Sueki, K., & Niino, H. (2016). Toward better assessment of tornado potential in typhoons: Significance of considering entrainment effects for CAPE. *Geophysical Research Letters*, *43*(24), 12597–12604. https://doi.org/10.1002/2016gl070349

Torn, R. D., & Snyder, C. (2012). Uncertainty of tropical cyclone best-track information. *Weather and Forecasting*, *27*(3), 715–729. https://doi.org/10.1175/waf-d-11-00085.1

Trier, S. B., Ahijevych, D. A., Carroll-Smith, D., Bryan, G. H., & Edwards, R. (2023). Composite mesoscale environmental conditions influencing tornado frequencies in landfalling tropical cyclones. *Weather and Forecasting*, *38*(12), 2481–2508. https://doi.org/10.1175/waf-d-22-0227.1

Verbout, S. M., Schultz, D. M., Leslie, L. M., Brooks, H. E., Karoly, D., & Elmore, K. L. (2007). Tornado outbreaks associated with landfalling hurricanes in the North Atlantic basin: 1954–2004. *Meteorology and Atmospheric Physics*, *97*(1–4), 255–271. https://doi.org/10.1007/s00703-006-0256-x

Waco, D. E. (1970). Temperatures and turbulence at tropopause levels over Hurricane Beulah (1967). *Monthly Weather Review*, *98*(10), 749–755. https://doi.org/10.1175/1520-0493(1970)098<0749:tatatl>2.3.co;2

Wang, J., Young, K., Hock, T., Lauritsen, D., Behringer, D., Black, M., et al. (2015). A long-term, high-quality, high-vertical-resolution GPS dropsonde dataset for hurricane and other studies. *Bulletin American Meteorology Social*, *96*(6), 961–973. https://doi.org/10.1175/bams-d-13-00203.1

Wang, Y., Yussouf, N., Kerr, C. A., Stratman, D. R., & Matilla, B. C. (2022). An experimental 1-km Warn-on-Forecast System for hazardous weather events. *Monthly Weather Review*, *150*(11), 3081–3102. https://doi.org/10.1175/mwr-d-22-0094.1

Waugh, S. (2024). NSSL mobile hurricane soundings [Data]. https://zenodo.org/records/10067475

Wheatley, D. M., Knopfmeier, K. H., Jones, T. A., & Creager, G. J. (2015). Storm-scale data assimilation and ensemble forecasting with the NSSL Experimental Warn-on-Forecast System. Part I: Radar data experiments. *Weather and Forecasting*, *30*(6), 1795–1817. https://doi.org/10.1175/waf-d-15-0043.1

Whitaker, J. S., Hamill, T. M., Wei, X., Song, Y., & Toth, Z. (2008). Ensemble data assimilation with the NCEP global forecast system. *Monthly Weather Review*, *136*(2), 463–482. https://doi.org/10.1175/2007mwr2018.1

Yussouf, N., Kain, J. S., & Clark, A. J. (2016). Short-term probabilistic forecasts of the 31 May 2013 Oklahoma tornado and flash flood event using a continuous-update-cycle storm-scale ensemble system. *Weather and Forecasting*, *31*(3), 957–983. https://doi.org/10.1175/waf-d-15-0160.1

Yussouf, N., Kain, J. S., & Clark, A. J. (2020). Probabilistic high impact rainfall forecasts from landfalling tropical cyclones using Warn-on-Forecast system. *The Quarterly Journal of the Royal Meteorological Society*, *146*(730), 2050–2065. https://doi.org/10.1002/qj.3779